3D surface displacements during the 2016 M_W 7.8 Kaikōura earthquake (New Zealand) from photogrammetry-derived point clouds

A. Howell[1†], E. Nissen[2], T. Stahl[3], K. Clark[4], J. Kearse[1,3,4], R. Van Dissen[4], P. Villamor[4], R. M. Langridge[4] and K. Jones[4]

[1]School of Geography, Environment and Earth Sciences, Victoria University of Wellington, New Zealand. [2]School of Earth and Ocean Sciences, University of Victoria, Victoria, B.C., Canada. [3]Department of Geological Sciences, University of Canterbury, Christchurch, New Zealand. [4]GNS Science, PO Box 30 368, Lower Hutt, New Zealand.

Corresponding author: Andy Howell (a.howell@gns.cri.nz)

†Current addresses: (1) Department of Geological Sciences, University of Canterbury, Christchurch, New Zealand; (2) GNS Science, PO Box 30 368, Lower Hutt, New Zealand.

Key Points:

- High-resolution, three-dimensional surface displacements during earthquakes can be measured from aerial photographs.
- The Jordan Fault did not accommodate significant shortening in an earthquake in 2016, but probably does in the long term.

Abstract

High-resolution, three-dimensional (3D) measurements of surface displacements during earthquakes can provide constraints on fault geometry and near-surface slip, and also quantify on- and off-fault deformation. However, measurements of surface displacements are often hampered by a lack of high-resolution pre-earthquake elevation data, such as lidar. For example, pre-earthquake lidar for the 2016 M_W 7.8 Kaikōura, New Zealand earthquake only covers ≲10% of ~180 km of mapped surface ruptures. To overcome a lack of pre-earthquake lidar, we measure 3D co-seismic displacements during the Kaikōura earthquake using point clouds generated from aerial photographs. From these point clouds, which cover the whole area of the 2016 surface ruptures, it is possible to measure 3D displacements to within ±0.2 m.

We measure co-seismic slip and estimate the geometries of faults in the steep, inaccessible Seaward Kaikōura mountains, where post-earthquake field observations are very sparse. The Jordan Fault (previously the Jordan Thrust) ruptured in 2016 as a moderate-to-steeply dipping (~50-80°), predominantly strike-slip fault. Slip on this fault in 2016 — which included a normal-sense component in some areas — contrasts with field observations that indicate significant longer-term shortening across the Jordan Fault during the Holocene. It is therefore likely that different earthquakes on the Jordan Fault have very different slip vectors, and that the fault does not exhibit "characteristic" slip behaviour. For faults like the Jordan Fault, long-term time-averaged estimates of slip rate may not be reliable indicators of the sense and magnitude of slip in individual earthquakes.

1. Introduction

In recent years, it has become possible to map surface displacements during earthquakes at sub-metre precision, using remote-sensing techniques such as InSAR and optical image correlation (e.g. Elliott et al., 2016). High-resolution maps of earthquake surface displacements have shown that ruptures are, in general, more complex than previously thought. For example, the rupture of multiple faults appears to be relatively common — although not universal — during large or great earthquakes. Notable recent examples of *multi-fault ruptures* captured using imaging geodesy include the 2010 El Mayor-Cucupah

earthquake (Lajoie et al., 2019; Oskin et al., 2012), the 2010 Darfield earthquake (Elliott et al., 2012; Duffy et al., 2013) and the 2018 Palu earthquake (Socquet et al., 2019). The focus of this study is the 2016 November 14 M_W 7.8 Kaikōura earthquake in New Zealand, which ruptured over 20 different faults (Litchfield et al., 2018a; Figure 1b).

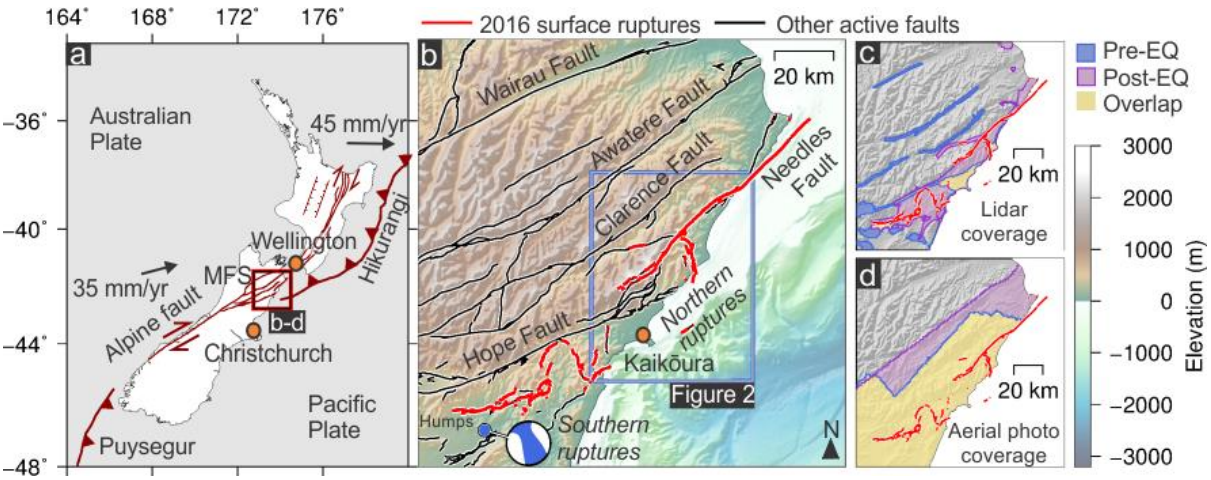

Figure 1. *Tectonic setting of the 2016 Kaikōura earthquake and spatial coverage of elevation data.* ***(a)*** *Tectonic setting of New Zealand. Major fault systems are marked by red lines; motions of the Australian Plate relative to the Pacific Plate (Beavan et al., 2002) are marked by black arrows. MFS: Marlborough Fault System.* ***(b)*** *Faults in the NE South Island of New Zealand. Black lines mark active faults (Langridge et al., 2016) and red lines show surface ruptures of the 2016 Kaikōura earthquake (as mapped by Litchfield et al., 2018a, 2018b). The 2016 epicentre (Kaiser et al., 2017) and Global Centroid Moment Tensor focal mechanism (Ekstrom et al., 2012) are shown in blue. Relief is from Mitchell et al. (2012).* ***(c)*** *and* ***(d)*** *Pre-earthquake and post-earthquake spatial coverage of lidar and our photogrammetry-derived point clouds.*

An earthquake that ruptures several faults together will almost always have a greater magnitude than an earthquake on one of the faults individually. From a seismic hazard perspective, it is therefore important to identify groups of faults that are able or likely to rupture together (e.g. Field et al., 2014). Such identification of potential future multi-fault ruptures clearly requires a detailed understanding of past multi-fault earthquakes (e.g.

Fletcher et al., 2014; Hamling et al., 2017). It is especially important to understand fault interactions and the ways that ruptures propagate between faults (Klinger et al., 2018).

Any model of stress transfer or rupture propagation between faults must depend on a model of fault locations and geometries (e.g. Ando and Kaneko, 2018; Ulrich et al., 2019). The slip distribution, location and geometry of a fault can be difficult to constrain, even after rupture in an earthquake (Ragon et al., 2018). It is particularly hard to disentangle the effects of slip on multiple faults (with poorly-constrained geometries) using seismologic methods or relatively sparse GNSS measurements (e.g. Kaiser et al., 2017). Consequently, for complex, multi-fault earthquakes, many of the best constraints on fault slip and geometry come from remote-sensing measurements of co-seismic surface displacements (e.g. Wei et al., 2011, Hamling et al., 2017).

The three main remote-sensing techniques used to measure surface displacements are: (1) satellite-borne Synthetic Aperture Radar Interferometry, or InSAR; (2) correlation of orthorectified aerial or optical satellite imagery; and (3) 3D differencing of point clouds, usually derived from lidar data. These techniques, although extremely useful, all have important limitations. Displacement measurements using InSAR are problematic close to faults or steep topography, or if there is a change in the back-scattering properties of the ground surface (Elliott et al., 2016). Optical image correlation can measure horizontal displacements accurately, but the resolution of vertical displacements, although fast improving, is significantly lower (Kuo et al., 2018; Zinke et al., 2019). It is possible to measure high-resolution 3D displacements from terrestrial or airborne lidar-derived point clouds (e.g. Nissen et al., 2012; Wedmore et al., 2019), but pre-earthquake lidar coverage is generally limited. Similarly, although pre-earthquake topographic models can be created from optical satellite imagery (Zhou et al., 2018; Barnhart et al., 2019), such models have much lower resolutions than lidar point clouds, leading to lower-quality displacement measurements.

In a first for a major earthquake, we use pre- and post-earthquake aerial photographs to constrain 3D surface displacements during the 2016 Kaikōura earthquake. Point clouds generated from these aerial photographs bridge the gap between: (1) lidar data, which have a very high point density but limited pre-earthquake spatial coverage in the Kaikōura

region (Figure 1c); and (2) point clouds derived from optical satellite imagery (e.g. Barnhart et al., 2019, Gold et al., 2019), which have good spatial coverage but a higher point spacing than our aerial photograph-derived point clouds (~2 m compared with 0.6 m). We first extract a 3D co-seismic displacement field from the point clouds using the iterative closest point (ICP) algorithm. Second, we validate our displacement field using lidar point clouds, field measurements and displacements derived from satellite imagery. Finally, we use our displacement field to measure near-surface slip on faults of interest and to constrain their geometry.

Our results demonstrate that reliable, high-resolution 3D co-seismic displacements can be extracted from photogrammetry-based point clouds. We show that such high-resolution displacement measurements can be used to (1) map surface ruptures accurately, especially in regions that are hard to access; (2) constrain co-seismic near-surface slip on faults; and (3) estimate fault geometry. To demonstrate the utility of the method, we map surface ruptures in the Seaward Kaikōura mountains (Figure 2a) and characterise 2016 slip on the poorly-understood Jordan Fault. The results indicate that the Jordan Fault (originally mapped as the "Jordan Thrust"; Van Dissen and Yeats, 1991) ruptured in 2016 as a moderate-to-steeply dipping, predominantly strike-slip fault.

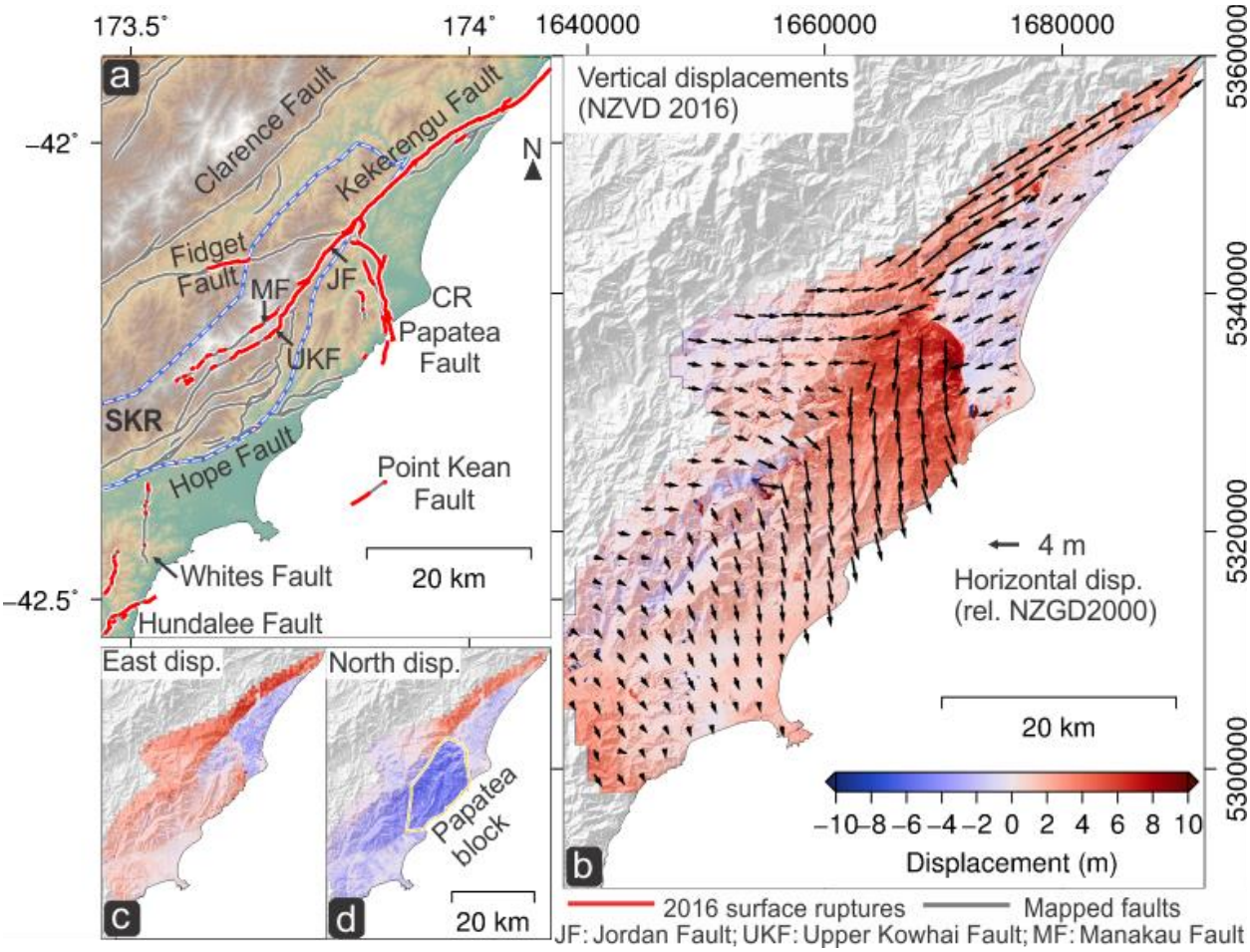

Figure 2. *3D displacements around the northern 2016 Kaikōura ruptures, calculated from photogrammetry-derived point clouds.* ***(a)*** *2016 surface ruptures (red, from Litchfield et al., 2018) and other active faults (grey, from Langridge et al., 2016). The Seaward Kaikōura Range (SKR) is delineated by a blue and white line. JF: Jordan Fault; MF: Manakau Fault; UKF: Upper Kowhai Fault; CR: mouth of the Clarence River.* ***(b)*** *Vertical (colour scale) and horizontal (vector arrows) displacements during the 2016 earthquake.* ***(c)*** *and* ***(d)*** *east and north displacements (same colour scale as (b)). The location of the Papatea block is marked by a gold line in (d).*

2. The 2016 Kaikōura earthquake

The 2016 November 14 Kaikōura M_W 7.8 earthquake occurred the northern South Island of New Zealand, rupturing several faults of the Marlborough Fault System (Figure 1a). The

Marlborough Fault System accommodates 35-40 mm/yr. of relative motion between the Pacific and Australian plates (Beavan et al., 2002). This motion is accommodated primarily through slip on the right-lateral Wairau, Awatere, Clarence, Kekerengu and Hope Faults (Figure 1b). The 2016 earthquake occurred close to the Hope Fault, which has one of the fastest late-Holocene slip rates of these faults (up to ~25 mm/yr.; Langridge et al., 2003; Little et al., 2018).

The Kaikōura earthquake nucleated on or near the Humps Fault (Figure 1b) and propagated northeast (Kaiser et al., 2017; Duputel and Rivera, 2017); it ruptured over 20 onshore and offshore faults with a wide variety of fault orientations and slip styles (Litchfield et al., 2018a). Almost half of the faults that ruptured during the earthquake had not been mapped previously, although most seismic moment was released on faults that had been mapped. Surprisingly, slip on the Hope Fault was minimal (<1 m; Litchfield et al., 2018a), despite: (1) its favourable orientation for the accommodation of relative Australia-Pacific plate motion in the region (Nicol et al., 2018); and (2) the rupture of similarly-oriented faults north and south of the Hope Fault (Figure 2a; Hamling et al., 2017).

The faults that ruptured in the Kaikōura earthquake can be divided spatially into two groups, separated by the Hope Fault (Figures 1b and 2a). The southern group (Figure 1) includes the Humps, Leader, Conway-Charwell, and Hundalee faults, among others (Litchfield et al., 2018; Nicol et al., 2018). The northern group of faults includes the Papatea, Kekerengu and Needles faults and several faults in the Seaward Kaikōura Range (Figure 2a; Kearse et al., 2018; Langridge et al., 2018; Litchfield et al., 2018). We focus on the northern group of faults because: (1) the greatest 2016 slip and seismic-moment release occurred on the northern faults (Hamling et al., 2017; Litchfield et al., 2018); and (2) faults in the Seaward Kaikōura Range are the hardest to access, and therefore most appropriate for a remote-sensing study.

Despite a wealth of data available for study of the Kaikōura earthquake, several aspects of the co-seismic slip distribution and slip evolution remain unclear. Three important and poorly-understood features of 2016 co-seismic slip are:

1. **Rupture propagation between the southern and northern faults.** Mapped surface ruptures for the northern and southern faults are separated by ~4.5 km and the Hope Fault (Litchfield et al., 2018a; Zinke et al., 2019) and it is not clear how the 2016 rupture propagated between them. Dynamic rupture models have suggested that the 2016 rupture either: (1) "jumped" 15-20 km from the Hundalee Fault to the Jordan Fault through dynamic-stress triggering (Ando & Kaneko, 2018); or (2) propagated along an offshore fault to the Papatea fault, before moving north to the Jordan-Kekerengu system (Klinger et al., 2018; Ulrich et al., 2019). A third possibility is that rupture propagated more directly between the Hundalee and Jordan faults by rupturing the onshore Whites and Snowflake Spur faults (Zinke et al., 2019). Different studies have used different fault geometries; better constraints on fault geometry are required to test and compare these different dynamic rupture models.
2. **The co-seismic behaviour of the Papatea block.** The region bounded by the coast, the Papatea Fault and the Jordan Fault (Figure 2a) is known as the Papatea block (Hamling et al., 2017; Langridge et al., 2018). The eastern part of the block was uplifted by ~8 m in 2016; it was also displaced by up to ~4 m horizontally (southwards relative to stable New Zealand; Hamling et al., 2017). Hamling et al. (2017) and Diederichs et al. (2019) suggested that uplift of the Papatea block in 2016 was predominantly anelastic, based on displacement measurements around the Papatea Fault that were poorly fit by elastic models. Co-seismic displacements and slip evolution along the northern boundary of the block remain poorly understood (Zinke et al., 2019).
3. **The long-term slip behaviour of the Jordan Fault**. Van Dissen and Yeats (1991) mapped a fault on the southern side of the Seaward Kaikōura mountains (Figure 2a). Their mapped fault has clear reverse-faulting offsets and dips NW at 25-48° (average dip 35°), and was consequently named the Jordan Thrust. Van Dissen and Yeats (1991) argued that slip on the Jordan

Thrust contributes to long-term uplift of the Seaward Kaikōura Range. However, offsets of the ground surface observed in 2016 in the region of the Jordan Fault were dextral-normal offsets. The north-west (hanging-wall) side of the fault subsided relative to the south-east (footwall) side. Normal offsets were significant (~4 m) at the fault's eastern end. It remains unclear whether the fault that ruptured in 2016 is also responsible for long-term uplift of the Seaward Kaikōura Range (Zinke et al., 2019).

To address these problems, a better understanding of the faults in the Seaward Kaikōura Range is required. In particular, reliable estimates of fault kinematics are necessary to inform and constrain models of rupture propagation and stress transfer. Accurate slip measurements on the Jordan Fault may also help understand: (1) its long-term behaviour; and (2) its role in accommodating southwards motion of the Papatea block. We aim to provide some of these constraints and measurements by building on work from previous remote-sensing studies.

2.1 Previous remote-sensing measurements of co-seismic displacements during the Kaikōura earthquake

Several remote-sensing techniques have been used to map surface displacements during and immediately after the 2016 Kaikōura earthquake. 3D surface displacements have been measured using: (1) SAR interferometry and pixel offsets; (2) optical image correlation (OIC); and (3) differencing of lidar point clouds.

InSAR provides many of the strongest constraints on the slip distribution of the Kaikōura earthquake (e.g. Hamling et al., 2017, Wang et al., 2018, Xu et al., 2018). InSAR studies were able to identify almost all of the major faults that ruptured in 2016, including for several fault segments with no surface ruptures. Different studies agree on most large-scale features of the distribution of surface displacements. Aspects of the 2016 slip distribution that remain controversial include: (1) the behaviour of the Papatea block during the earthquake; and (2) slip on faults that project to the surface offshore, including the Australia-Pacific subduction interface (Hamling et al., 2017, Wang et al., 2018, Xu et al., 2018).

Several studies have used sub-pixel optical image correlation to measure surface displacements during the Kaikōura earthquake (e.g. Hollingsworth et al., 2017; MacKenzie et al., 2017; Klinger et al., 2018; Zinke et al., 2019). It is possible to identify major faults and measure displacements ≳ 1 m using ~10-m resolution satellite imagery such as Landsat (e.g. Hollingsworth et al., 2017), but higher-resolution optical imagery is required to measure smaller displacements. Using ~0.5-m resolution Pleiades and Worldview imagery, Klinger et al. (2018) and Zinke et al. (2019) were able to measure horizontal surface offsets on faults to within ±0.2-0.3 m. Zinke et al. (2019) mapped a previously unidentified fault (the Snowflake Spur Fault) in the Seaward Kaikōura Range. MacKenzie et al. (2017) and Zinke et al. (2019) also calculated vertical displacements from satellite imagery. The accuracy of these vertical displacement measurements is lower than for horizontal displacements (typically ≳ 0.7 m), but Zinke et al. (2019) were able to measure vertical offsets to within ±0.3 m in some places.

Where pre-earthquake lidar coverage exists (Figure 1c) — a narrow strip along the coast, the coastal part of the Clarence Valley (the river mouth is labelled in Figure 2a) and parts of the southern 2016 ruptures — differential lidar provides valuable constraints on surface displacements. Clark et al. (2017) and Mouslopoulou et al. (2019) used high-resolution elevation changes derived from lidar digital surface models (DSMs) to supplement field measurements of uplift along the coast and constrain slip on faults where they cross the coastline. Diederichs et al. (2019) used the iterative closest point (ICP) algorithm to extract 3D displacements in the lower Clarence Valley from pre-earthquake and post-earthquake lidar point clouds. They measured 3D offsets on the Papatea Fault (Figure 2a) to within ±0.2 m, inferring a sub vertical (~90°) dip at the northern end of the fault. Nicol et al. (2018) and Langridge et al. (2018) used differential lidar elevation changes to map faults and measure vertical displacements around parts of the Humps, Hope and Papatea faults.

Our study is the first use of point clouds derived from aerial photographs to measure 3D surface displacements over the 2016 Kaikōura ruptures; however, Van Dissen et al. (2019) did apply the same technique in a few small (~400 m-wide) regions to examine strains around individual buildings. The current study is also — to our knowledge — the first use of aerial photographs to measure 3D surface displacements during a major earthquake.

Several studies have presented 2D co-seismic displacements derived from aerial photographs (e.g. Milliner et al., 2016; Ekhtari and Glennie, 2017) and recent studies have measured 3D displacements from optical satellite imagery (e.g. Kuo et al., 2018; Zhou et al., 2018; Barnhart et al., 2019; Zinke et al., 2019). In general, the optical satellite images used in these studies have lower resolutions than our aerial images, resulting in lower-density point clouds. For example, Barnhart et al. (2019) used digital surface models with 2 m resolution for their ICP study, compared with a 0.6-m mean point spacing for our point clouds. The resolution of displacements from optical image correlation depend more directly on the resolution of available imagery; Zinke et al. (2019) used 0.3-m and 0.5-m satellite images, but filtered them to give pre-and post-earthquake imagery with 1-m resolution.

3. Methods

3.1 Construction of point clouds from aerial photographs

The principal data used in this study are pre- and post-earthquake point clouds derived from 2014-2015 and November 2016-2017 aerial photographs of the Kaikōura region (total area ~3000 km^2; coverage in Figure 1b) collected by Aerial Surveys Ltd. Photographs were taken from a fixed-wing aircraft flying at ~5800 m, with sufficient image resolution, stereo overlap (60% forward overlap) and ground control to create a 0.3-m resolution orthophoto.

Pre- and post-earthquake point clouds were constructed by Aerial Surveys Ltd from the relevant aerial photographs using standard stereo techniques and Intergraph ISAE-ext software. Approximately 180 ground control points (GCPs) were used to anchor each point cloud. Apart from a few Land Information New Zealand (LINZ) survey benchmarks, GCPs were concentrated close to the coast and near major roads (for reasons of accessibility), in sites with flat, open topography. For both the pre- and post-earthquake datasets, the mean point spacing of the densely-matched point cloud is ~0.6 m.

The uncertainty in the horizontal position of each cloud at the 95% confidence level, relative to New Zealand Geodetic Datum 2000, is ±2 m. However, there is good agreement between our calculated horizontal displacements and those measured using other

techniques (discussed in Section 4.2). For example, the median differences between lidar-derived and photogrammetry-derived east and north displacements are 0.41 m and 0.79 m respectively. It is therefore likely that any *relative* horizontal differences between the registration of our pre- and post-earthquake point clouds are smaller than 2 m.

Elevations within our point clouds are relative to New Zealand Vertical Datum 2016. To test the vertical registration of our photogrammetry-derived point clouds, we grid them and compare the resulting 1-m digital surface models (DSMs) with lidar-derived DSMs. We restrict our detailed vertical comparison to the region immediately inland of the Clarence River mouth (Figure 2a), the largest contiguous region where: (1) pre- and post-earthquake lidar overlap; and (2) a range of vertical displacements were observed during the 2016 earthquake. To exclude the effects of vegetation and steep slopes from our vertical differencing, we consider only elevations in flat areas without trees, away from the Clarence river bed.

In the areas where comparisons were made, there is good agreement between the elevations of the post-earthquake (2017) lidar-derived and photogrammetry-derived DSMs; the mean vertical difference is 0.06 m, with a standard deviation of 0.2 m. However, these same flat areas in the pre-earthquake (2015) photogrammetry-derived DSM are consistently lower than in the pre-earthquake lidar DSM; the mean difference is 0.6 m, with a standard deviation of 0.3 m. We attribute these differences to misregistration of ground control points. Vertical differences between the pre- and post-earthquake lidar DSMs agree with coastal uplift measurements (Clark et al., 2017) and GPS-measured vertical offsets (Hamling et al., 2017), so we assume that the elevations in the pre-earthquake lidar DSM are correct. There is no clear spatial trend in the difference between the lidar-derived and photogrammetry-derived DSMs, so we apply constant vertical corrections to our pre-earthquake point clouds.

3.2 Calculation of 3D displacements using the ICP algorithm

In the following analysis, in the interests of brevity, we refer to the displacements observed between the pre- and post-earthquake aerial surveys as co-seismic displacements. The last post-earthquake aerial images were captured in mid-February 2017 (~3 months after the

earthquake), so our calculated displacements also include some post-seismic deformation over that interval. However, post-seismic displacements observed using InSAR and GPS over the same interval were much smaller than co-seismic displacements (Wallace et al., 2018). In most parts of the northern 2016 ruptures, total post-seismic displacements before March 2017 were <0.2 m (Hamling et al., 2017; Wallace et al., 2018). These post-seismic displacements were less than 10% of co-seismic displacements, which were >2 m throughout the northern 2016 ruptures.

We use an adaptation of the iterative closest point algorithm (ICP; Besl & McKay, 1992; Chen & Medioni, 1992) to retrieve the 3D deformation field that matches our 2014-2015 point cloud to our 2016-2017 point cloud. The use of this algorithm to extract co-seismic displacements from pre-and post-earthquake lidar point clouds is now fairly routine and described in detail elsewhere (e.g. Ekhtari & Glennie, 2018; Nissen et al., 2012, 2014; Scott et al., 2018). Our purpose is not to test the ICP algorithm. Rather, we aim to demonstrate the utility of the algorithm beyond lidar, by showing that co-seismic 3D displacements can be measured from aerial photogrammetry-derived point clouds. Our implementation of point-to-plane ICP is very similar to those of Nissen et al. (2014), Scott et al. (2018) and Diederichs et al. (2019); we refer the reader to those studies for discussions of the basic principles of the technique.

The "windowed" implementation of the ICP algorithm divides the pre- and post-earthquake point clouds into a regular east-west grid of windows or "cells" (Nissen et al., 2012). In this study, we divide the pre-earthquake point cloud into 50 m by 50 m square cells centred 25 m apart, so that each cell overlaps by 25 m with each of its neighbours. The use of overlapping cells allows us to retrieve a higher-resolution deformation field while ensuring that each cell contains sufficient points for a reliable displacement measurement (Ekhtari & Glennie, 2018; Nissen et al., 2012). Our approach yields independent, 3D displacement measurements every 50 m. For comparison, the OIC approach of Zinke et al. (2019) uses a 32 × 32 pixel moving window to measure displacements from 1-m resolution images, over an 8-m grid; that approach results in independent displacement measurements every 32 m (a slightly higher resolution than our displacement field).

For each cell centre point in our 25 m grid, we use the ICP algorithm to obtain the 3D rigid-body transformation that matches the topographies of pre-earthquake and post-earthquake cells centred on that point. The post-earthquake cell has larger dimensions (70 by 70 m) than the pre-earthquake cell (50 by 50 m); this allows for the possibility of up to 10 m of horizontal co-seismic displacement in each of the east-west and north-south directions. For horizontal displacements smaller than ~10-14 m (depending on the direction of displacements), all of the topographic features in the pre-earthquake cell should also be included in the post-earthquake cell.

The adaptation of the ICP algorithm that we use (Diederichs et al., 2019) allows for the use of sparse ICP (Bouaziz et al., 2013), to help deal with noisy, sparse data. The sparse ICP implementation adjusts the weights of outliers and points in gaps between successive iterations of the ICP algorithm, depending on the value of a parameter p. Although photogrammetry-derived point clouds are often noisy, most of the noise in our displacement field is either at long wavelengths or from identifiable sources (discussed in Section 4.1). We therefore set p to 1.8, equivalent to a minimal correction for noise and data gaps (Bouaziz et al., 2013; Diederichs et al., 2019). Experimenting with p has a minimal effect on our calculated displacement field; this is probably because point spacing is relatively even (few data gaps) and there is relatively little noise at short wavelengths.

3.3 Measurement of surface offsets

We estimate co-seismic near-surface slip on several faults of interest, using the 3D displacement field discussed in Section 3.1 and shown in Figure 2. In the following discussion, the term *displacement measurement* refers to the 3D displacement of a 50 × 50 m window estimated using the ICP algorithm. The term *offset measurement* refers to the motion of one side of a fault relative to the other side of the fault. These co-seismic *offsets* are estimated from cross-fault swath profiles through the displacement field, similar to previous lidar-based studies (e.g. Lajoie et al., 2019; Diederichs et al., 2019).

The spacing of our offset measurement sites varies depending on terrain and land cover. We determine exact locations of measurement sites manually, using aerial orthoimages and the 2017 bare-earth lidar DEM to avoid sites where (for example) landslides and changes

in vegetation might hinder measurements of tectonic displacements. Where topography and land cover permit the even spacing of measurement sites, we measure offsets at 500 m intervals along a simplified surface-rupture trace. At each site, we measure offsets along a 1000 m-long profile, centred on a simplified fault trace and oriented perpendicular to the local strike of the fault (an example is shown in Figure 3). We project displacement measurements from a 200 m-wide swath onto the profile. This swath width and profile length allows a maximum of ~180 displacement measurements on each side of the fault to calculate the average displacements.

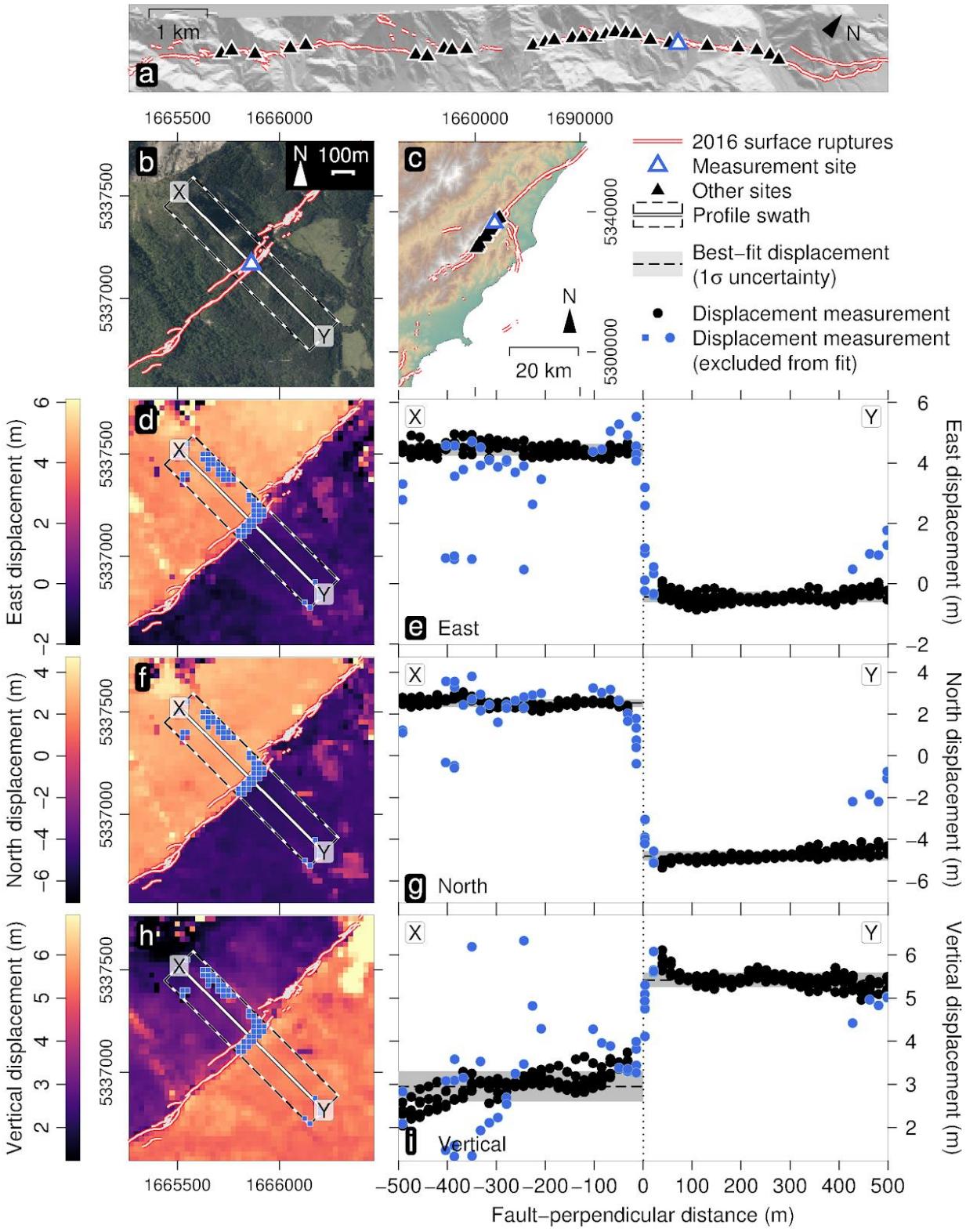

Figure 3. *Illustration of the technique used to measure offsets across faults, for a site on the Jordan Fault.* ***(a)*** *Map of surface ruptures (red lines) and measurement sites (triangles) along*

the Jordan Fault. A blue triangle marks the measurement site of interest. ***(b)*** *Aerial orthoimage of the measurement site.* ***(c)*** *Map showing the location of measurement site relative to the northern 2016 ruptures.* ***(d)*** *Map view of displacements in the E-W direction (eastwards is positive). The region from which displacements were projected onto a profile is shown by a dashed line.* ***(e)*** *Profile of projected E-W displacements. Points that were not used to calculate offsets are shown in blue; in this case, we removed points within ~50 m of the fault and regions that had been displaced by landslides. Best-fitting mean displacements on each side of the fault (dotted line) are shown by dashed lines and 1σ uncertainties are shown in grey.* ***(f)*** *and* ***(g)*** *are equivalent to (d) and (e) for N-S displacements.* ***(h)*** *and* ***(i)****: map and profile of vertical displacements.*

We remove identifiable sources of noise from the profiles manually, using a dedicated graphical user interface. Examples of identifiable sources of noise (discussed in Section 4.1) include fast-growing trees, landslides and flat regions where the ICP algorithm cannot retrieve horizontal displacements. We also remove some measurements close to faults, where either: (1) off-fault deformation appears to be significant; or (2) the 50 × 50 m window of the pre-earthquake point cloud includes points on both sides of the fault. We only remove anomalous measurements for which we can identify a source of noise. If the reason for an anomalous displacement measurement is unclear, we include it in our fault-offset calculations so that the anomaly contributes to measurement uncertainty.

When calculating offsets across faults, we assume that over half the length of the swath profile (500 m), tectonic displacements do not vary significantly with distance from the fault. For each profile swath, we calculate the mean displacements in each of the east, north and vertical (up) directions on each side of the fault. The offset in a given direction is the difference between the mean displacements on either side of the fault, after outliers had been removed from the dataset (we will discuss the removal of noise in Section 4). Uncertainties in offsets are calculated by combining the variance of measurements on both sides of the fault (see Section S1). Where appropriate, we resolve east and north components of offsets into fault-parallel and fault-perpendicular horizontal offsets (heave);

our method for calculation of fault-parallel and fault-perpendicular uncertainties is described in the supplementary material.

4. Validation of 3D co-seismic displacements

Our calculated 3D displacements for the northern Kaikōura ruptures are shown in Figure 2b-d. The displacement field is smooth and shows clear discontinuities along surface ruptures, but also includes some non-tectonic displacements. Before comparing our results with displacements calculated using other methods, we consider these non-tectonic signals and (where appropriate) correct our dataset.

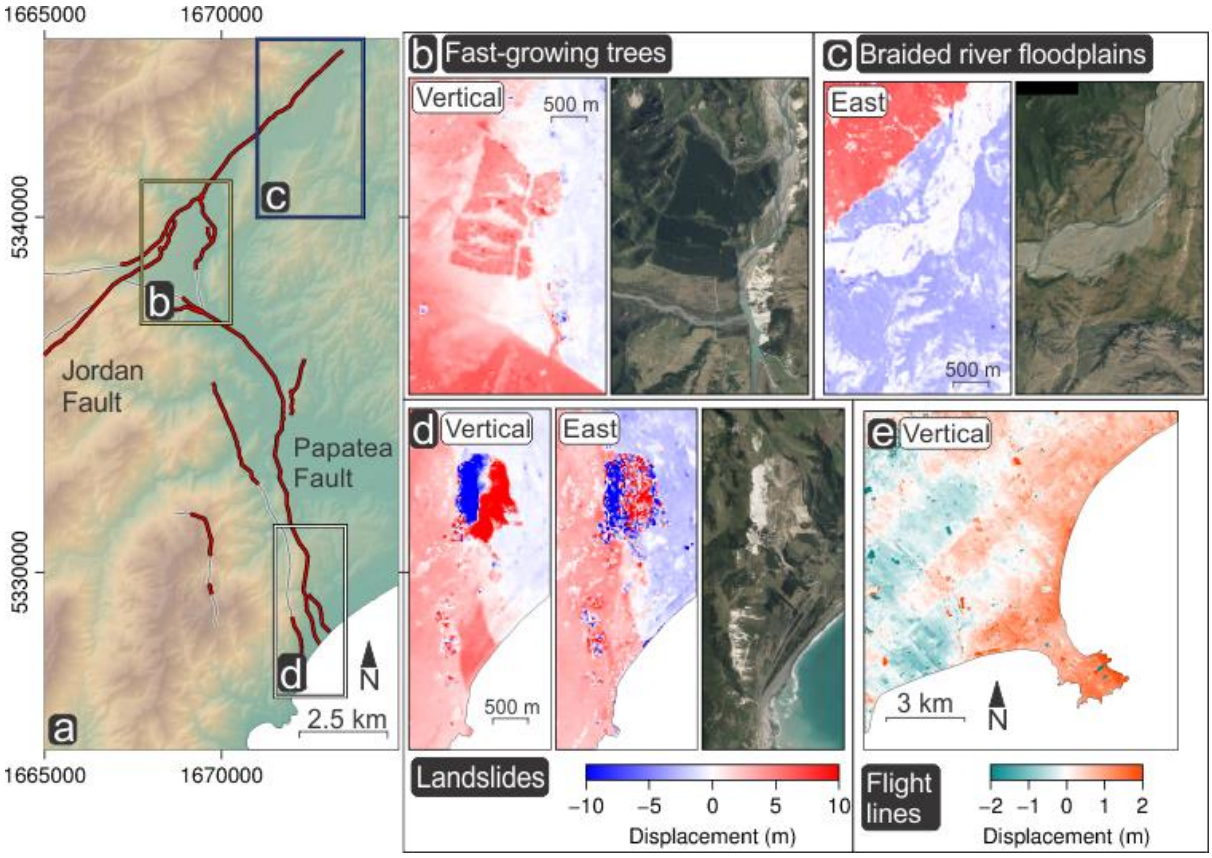

Figure 4. *Major sources of noise in our 3D displacement field.* ***(a)*** *Map showing 2016 surface ruptures in our region of interest (red lines) and locations of other maps in the figure. The colour scale is the same for (b) to (d).* ***(b)*** *Effect of the growth of pine trees on our vertical displacement field.* ***(c)*** *The braided floodplain of the Clarence River, where the ICP algorithm*

cannot measure horizontal displacements (only the eastward component of our displacement field is shown). ***(d)*** *Vertical and eastward displacements associated with the Seafront landslide on the Papatea Fault.* ***(e)*** *Flight-line distortions in our vertical displacement field on Kaikōura Flat (this area lies southwest of (a)). The peak-to-trough amplitude of the distortions is 0.7 m.*

4.1 Sources of noise and uncertainty in results

Sources of uncertainty in our displacements are illustrated in Figure 4 and include:

Fast-growing trees. Our pre-earthquake and post-earthquake aerial images were captured in 2014-2015 and 2016-2017 respectively. Since these point clouds include vegetation, changes in vegetation cover or height between our pre-earthquake and post-earthquake point clouds can affect our measured displacements. However, in most places where there is dense tree cover, the rate of growth of (predominantly native) trees is too slow to be a significant source of noise. Furthermore, in most vegetated areas where we measured co-seismic offsets across faults, the vegetation is of the same type (and therefore growing at similar rates) on both sides of the fault. Therefore, in most cases we assume that the contribution of vegetation growth to measured displacements is minimal.

The main areas where rapid tree growth disrupts our vertical displacement field are forestry plantations like the one shown in Figure 4b. Most of these plantations consist of *Pinus radiata* (Monterey Pine) trees, which can grow at rates of over 2 m/year, even when relatively mature (Linder et al., 1987). We remove areas classified as "Exotic Forest" in the New Zealand Land Cover Database (version 4.1; https://lris.scinfo.org.nz/) from our vertical displacement field.

Landslides. The 2016 Kaikōura earthquake generated over 10 000 landslides (Massey et al, 2018). The displacements associated with these landslides, although reasonably coherent (Figure 4d), are a major source of noise in the tectonic displacement field. Landslides in the region of interest have been mapped in detail as part of version 2 of the GNS landslide inventory (Massey et al., 2018). We remove areas classified as source areas or debris trails in the landslide inventory from the east, north and vertical components of

our displacement field. In some (~150) areas, we observe 3D displacements consistent with landsliding that are not included in the landslide inventory. However, such displacements are small (<0.5 m) and have a minimal effect on our results; we do not remove these areas from our displacement field.

Flat areas and river floodplains. One weakness of the windowed ICP algorithm — compared to, for example, InSAR or optical image correlation — is in measuring displacements in areas with flat topography (Scott et al., 2018). The algorithm solves for 3D displacements by matching topographic features in windows of the pre-earthquake and post-earthquake point clouds. If both the pre-earthquake and post-earthquake topography are flat (or planar, such as on gently-sloping hills), no horizontal displacement is required for the ICP algorithm to match the pre-and post-earthquake point clouds. In flat or planar areas, our implementation of the algorithm yields a horizontal displacement of zero; the resulting 3D displacement measurement is equivalent to a simple vertical differencing. Similarly, in some areas (such as on the rocky floodplains of braided rivers), the topography is not recognisable between the pre-earthquake and post-earthquake point clouds (Figure 4c). The ICP algorithm also retrieves horizontal displacements of zero in these areas.

In 2016, almost all of the northern Kaikōura ruptures experienced multi-meter horizontal displacements (relative to stable New Zealand) in a variety of directions (Hamling et al., 2017; Klinger et al, 2018). We therefore assume that where the measured net horizontal displacement is zero, the ICP algorithm has failed to retrieve a 3D displacement from the point cloud. Following a comparison of our measured displacements with those from other sources, we exclude all regions with a horizontal displacement of <0.5 m from our dataset. A careful inspection of our point clouds and calculated displacements indicates that this exclusion is reasonable. In areas of farmland, the ICP algorithm yielded realistic horizontal displacements for areas with small topographic features such as buildings and hedgerows. For flat fields immediately adjacent to these topographic features, horizontal displacements close to zero are retrieved.

Flight lines. Long-wavelength distortions to our calculated vertical displacements are visible in flat areas (e.g. Figure 4). These distortions, which trend NE-SW, are aligned with

the flight paths of the aircraft that captured the aerial imagery. The distortions (or *flight lines*) may be due to uncertainties in one of: (1) the camera position when images were captured; (2) lens parameters; or (3) the camera orientation, and in particular aircraft roll.

Comparisons between lidar-derived and photogrammetry-derived DSMs indicate that the effects of flight lines are greater for the pre-earthquake (2014-2015) point cloud than the post-earthquake point cloud. It would be possible to correct the point clouds for these long-wavelength distortions using lidar data. However, such a correction would only apply to areas with lidar coverage, away from the faults of interest in the Seaward Kaikōura Range. Furthermore, non-tectonic displacement discontinuities also exist in the lidar-derived point clouds (e.g. Glennie et al., 2014; Lajoie et al., 2019); a correction using lidar might simply introduce different artefacts to our point clouds. We attempted a correction using a national 8-m digital elevation model, but there are many differences at the sub-metre scale between our photogrammetry-derived DSM and the 8-m DEM.

We investigate the impact of flight lines by fitting sinusoidal functions to filtered swath profiles through our vertical displacement field (details in Section S2). These profiles show that distortions are smooth (they fit a sinusoidal curve well) and occur over a very consistent wavelength of 3100±100 m. The peak-to-trough amplitude of distortions reaches a maximum of 0.7 m close to the Kaikōura Peninsula (Figure 4e), but is typically $\lesssim$0.3-0.4 m. Distortions associated with flight lines appear to be smaller in mountainous regions than in low-lying, flat areas; this discrepancy may be due to a smaller difference between terrain elevation (1500-2800 m in the Seaward Kaikōura Range) and photo capture elevation ($\sim$5800 m).

We choose not to apply any correction for flight lines, since it is hard to measure their effects in several areas of our displacement field. We assume that the effects of flight lines on our measurements of fault offsets are minimal, given that:

1. The peak-to-trough amplitude of flight-line distortions is $\lesssim$0.6 m everywhere, which is significantly smaller than most vertical offsets across the faults of interest.

2. The length of the swath profiles that we use to measure offsets is 1000 m, which is smaller than the wavelength of flight-line distortions (3100±100 m).
3. The flight lines are oriented SW-NE, so the effective wavelength of distortions will be increased for offset measurements across faults that do not strike SW-NE.

Since we do not apply any correction, flight-line distortions will be translated into increased uncertainties in our fault offset estimates.

4.2 Comparison with displacements from other geodetic techniques

As a form of validation of our differencing technique, we now compare these measured displacements with results from other remote-sensing techniques and also field measurements. Each of the horizontal displacement vectors in Figure 2d shows the median horizontal displacement of a 2 km by 2 km area. Landslides and areas with horizontal net displacements <0.5 m were removed from the horizontal displacement field before calculating these median vectors. We also removed coastal areas of "new land" that were uplifted above mean sea level in 2016 (see Clark et al., 2017), since the pre-earthquake point cloud does not cover those areas.

One obvious comparison to make is between our results and those derived from ICP differencing of lidar point clouds. Several studies have demonstrated that, where differential lidar data exist, the ICP algorithm can extract reliable, high-resolution 3D displacements (Nissen et al., 2012, 2014; Scott et al., 2018; Ekhtari and Glennie, 2018, Lajoie et al., 2019).

A comparison between our photogrammetry-derived displacements and the lidar-derived displacement field of Diederichs et al. (2019) is shown in Figure 5. The lidar differencing workflow was almost identical to the workflow we described in Section 3.2; 3D displacements were measured over the same 25-m grid, using a 50 × 50 m pre-earthquake window and a 70 × 70 m post-earthquake window. There are some small, systematic differences between our measured displacements and those of Diederichs et al. (2019). These differences are presumably caused by differences between the registration of pre- and post-earthquake point clouds to New Zealand Geodetic Datum 2000. GPS

measurements of co-seismic displacements are not available for the region of interest, so it is difficult to determine the "correct" co-seismic displacement field. To facilitate comparison with the displacements of Diederichs et al. (2019), we shift our displacement field by 0.41 m and 0.79 m in the east and north directions respectively (the median differences between the displacement fields).

After these differences in registration are accounted for, differences between our horizontal displacement field and that of Diederichs et al. (2019) are small (Figures 5b-c and S4-5). The mean magnitude of the residual horizontal vectors in Figure 5d is 0.47 m. The lidar differencing is more effective at measuring horizontal displacements in flat areas such as fields. This better performance may be due to a greater number of narrow topographic features (such as fences) in the lidar point clouds. Alternatively, the higher point density and better vertical precision of the lidar point clouds (compared with our photogrammetry-derived point clouds) may also facilitate the detection and alignment of subtle topographic features. Differences between the lidar-derived and photogrammetry-derived vertical displacement fields (Figures 5c) are more pronounced, but still small. Most of the long-wavelength vertical differences are due to flight lines in both point clouds, and are $\lesssim$0.5 m. For the areas not affected by landslides, the mean residual between the lidar- and photogrammetry-derived vertical displacements is 0.23 m.

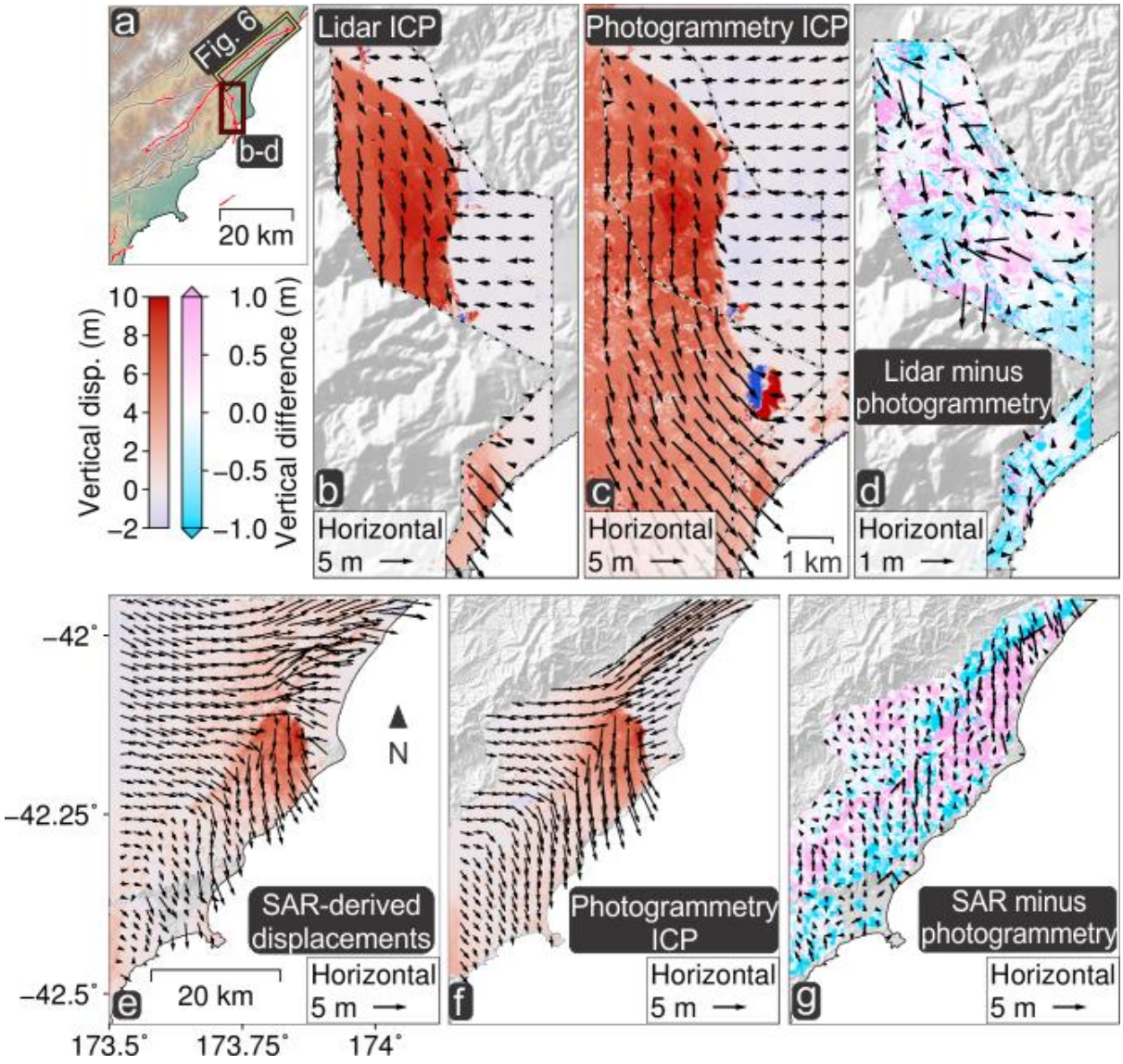

Figure 5. (a) *Map showing the location of (b) to (d).* ***(b)*** *Vertical (colour scale) and horizontal (vectors) displacements derived from lidar ICP.* ***(c)*** *Displacements derived from photogrammetry ICP.* ***(d)*** *Vertical and horizontal differences between lidar and photogrammetry ICP. Note that horizontal difference vectors are exaggerated in size by a factor of 5 relative to (b) and (c).* ***(e)*** *Vertical and horizontal SAR-derived displacements.* ***(f)*** *Displacements derived from photogrammetry ICP, averaged to show median displacements at the same resolution (4 arc-seconds) as SAR displacements.* ***(g)*** *Differences between SAR-derived and photogrammetry-ICP displacements. Note that unlike for (d), vector magnitudes in (g) are not exaggerated.*

The spatial extent of pre-earthquake lidar coverage of the Kaikōura surface ruptures is limited (Figure 1c). To assess the reliability of our measured displacements over the whole of the northern Kaikōura ruptures, we compare them with displacements measured using SAR interferometry and pixel offsets. Hamling et al. (2017) calculated the 3D displacements in Figure 5e from InSAR line-of-sight displacements and range and azimuth offsets, with a resolution of 15 arc seconds (~500 m).

There is good agreement between our displacements and the InSAR displacements (Figures 5e-g and S4-5). The mean residual between the vertical displacement fields is 0.06 m (standard deviation 0.89 m). The mean residuals between east and north displacements are 0.08 m (standard deviation 0.71 m) and 0.35 m (standard deviation 1.35 m) respectively. Note that unlike our comparison with the lidar-derived displacements, this comparison with InSAR results does not involve a correction for differences in registration of displacement fields.

The InSAR displacement field is noisier than our photogrammetry-derived displacement field, probably for two reasons. First, the InSAR displacements include the effects of landslides. Second, our displacements have been filtered to compare the results at the same resolution; we compare InSAR displacements with the median photogrammetry-derived displacements in each 15 arc second block. In general, there are few systematic differences between the InSAR-derived and photogrammetry-derived displacements (Fig. 5g).

The only region where our displacement field does differ systematically from the InSAR-derived displacements is in the NE of our study area, around the Kekerengu Fault (Figure 2a). InSAR results predict vertical uplift on both sides of the fault (Figure 5e). However, relative to our vertical displacement field, InSAR measures *more* uplift on the SE (coastal) side of the fault and *less* uplift of the NW side (Figure 5g). This disparity is equivalent to a systematic difference of 0.5-1 m in vertical offsets across the Kekerengu Fault. Our measured vertical and horizontal offsets agree well with field measurements and results from optical image correlation (Section 4.3). We therefore assume that our displacement field captures vertical offsets across the Kekerengu Fault reliably.

Similarly, there are differences between the north-south components of the photogrammetry-derived and InSAR-derived displacement fields around the Kekerengu Fault (Figure S5). Our results measure a southward co-seismic movement of the region immediately south of the Kekerengu, whereas the InSAR-measured displacement field suggests a *northward* movement of the same region. The reasons for these differences are unclear; however, other InSAR studies (Wang et al., 2018; Xu et al., 2018) also measure a southward co-seismic movement of the region south of the Kekerengu Fault.

4.3 Comparison with measured surface offsets

As a further validation of our results, we compare offsets across faults estimated using the method in Section 3.3 with: (1) field measurements of surface offsets on the fault (Kearse et al., 2018); and (2) 3D offsets across the fault derived from optical image correlation (Zinke et al., 2019). We restrict our comparison to the Kekerengu Fault, which is relatively accessible and has a good density of field slip measurements. Figure 6 shows our results and those of Zinke et al. (2019) resolved into vertical and fault-parallel (right-lateral) components to facilitate comparison with field measurements.

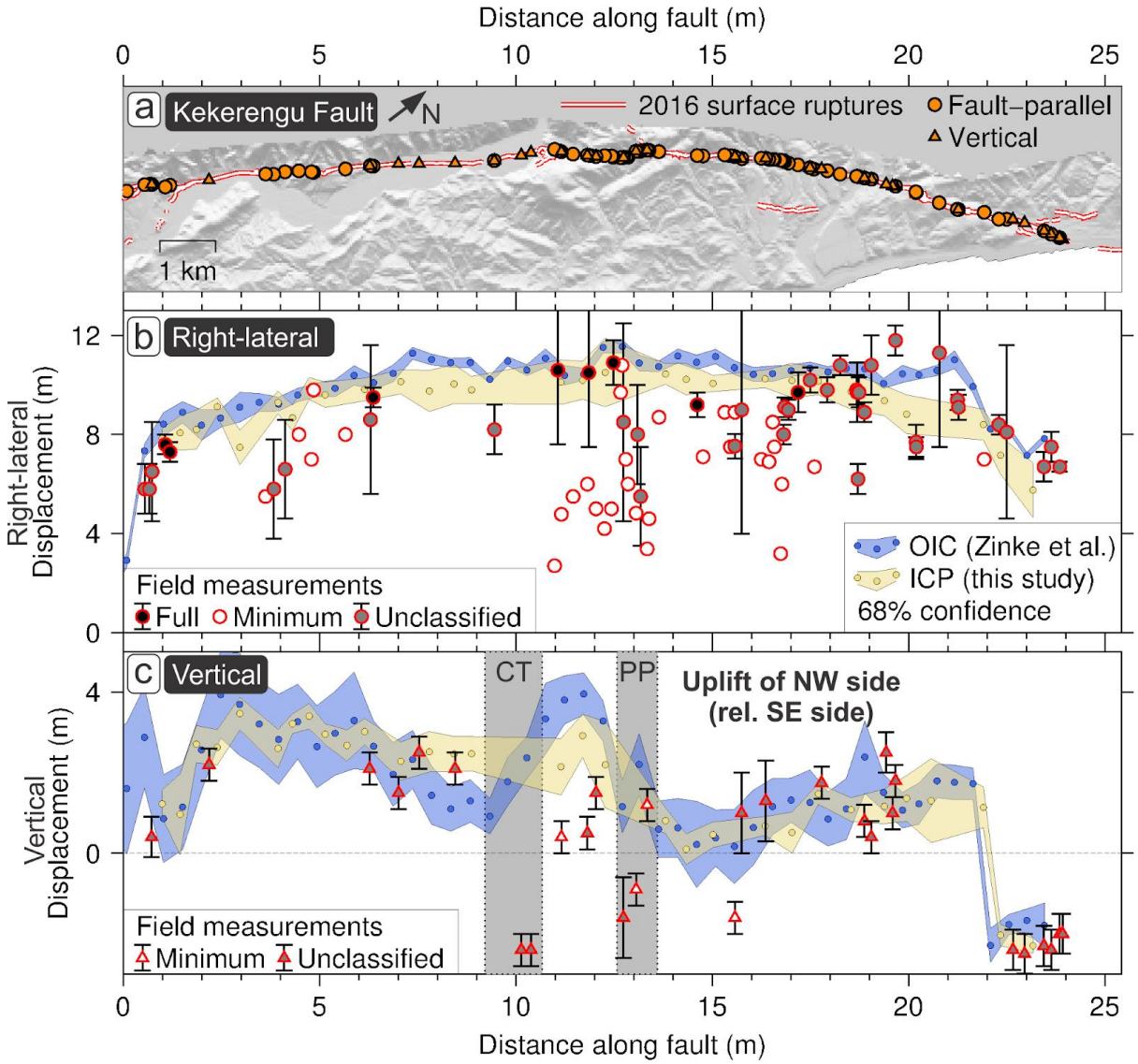

Figure 6. *Comparison of our measured offsets with those from field surveys (Kearse et al., 2018) and optical image correlation (OIC; Zinke et al., 2019).* ***(a)*** *Map of field measurement sites and surface ruptures (red lines) along the Kekerengu fault. Sites where horizontal displacements were measured are marked by circles; vertical measurement sites are represented by triangles.* ***(b)*** *Horizontal offsets. Black circles ("full measurements") show field offsets likely to capture all slip across the fault zone, with apertures of offset measurements that are typically ≳50 m. "Minimum" slip measurements are shown by white-filled circles; these measurements capture slip across only part of the fault zone (for example, an aperture ≲5 m or one of several strands). Offset measurements from OIC are shown in blue, with a 68% confidence envelope. Our measured offsets are shown in yellow.* ***(c)*** *Vertical offsets. Symbols*

are the same as for (b), except that field measurements are represented by triangles. CT: a region where we cannot measure near-fault deformation because of a corrupted 1 km x 1 km tile in the pre-earthquake point cloud. PP: a region where the fault passes through a pine plantation and vertical offsets are poorly constrained.

There is good agreement between the offsets measured using different methods. In general, the remote-sensing measurements of offsets are greater than the field measurements. There are two main reasons for these differences. First, many of the field measurements only measure offsets across one of several fault strands in a narrow (<30 m-wide) fault zone (see Kearse et al., 2018 for detailed maps of surface ruptures); consequently, these measurements underestimate net slip. By contrast, our ICP results rarely capture slip on different fault strands, because: (1) the resolution of our displacement field is 25 m; and (2) we remove near-fault data when measuring offsets.

Second, for many offset features (such as tree roots and farm tracks), it was only possible to measure offsets over a small aperture (~0.1-5 m either side of the fault). Such measurements do not account for off-fault deformation — which is often significant (e.g. Duffy et al., 2013; Milliner et al., 2016; Scott et al., 2018; Zinke et al., 2019) — and therefore also represent minimum estimates of total offsets (Kearse et al., 2018). In Figure 6, white-filled symbols represent these minimum estimates of offsets. Measurements that capture offsets over a wider aperture (~20-100 m; Kearse et al., 2019) are marked by black-filled circles in Figure 6b. These "full" offsets agree with both sets of remote-sensing measurements.

For horizontal offsets (Figure 6b), uncertainties derived from profiling our ICP displacement field are generally greater than those derived from optical image correlation (OIC) data. These greater uncertainties are unsurprising for two reasons. First, the OIC measurements were calculated at a higher spatial resolution than our ICP measurements and were also filtered more (Zinke et al., 2019). Second, there are few topographic features in much of the grassland around the Kekerengu Fault, so that the ICP algorithm does not always retrieve horizontal offsets reliably. In these flat, grassy areas, the "texture" of the

reflectance images used in OIC exceeds the topographic "texture" of our point clouds; it is therefore unsurprising that OIC performs better. Nonetheless, where land cover and terrain are suitable, uncertainties on our horizontal displacements are comparable with those from OIC (~0.2-0.3 m; 68% confidence).

For vertical offsets (Figure 6c), uncertainties on our measurements are significantly smaller than those of Zinke et al. (2019), whose vertical displacement field is noisier than ours. Zinke et al. (2019) suggest that their poor vertical resolution is because satellite viewing angles were close to nadir (downward-looking). The resolution of our vertical offset measurements is similar to our horizontal resolution (0.2-0.5 m in Figure 6c). The smallest vertical uncertainties calculated by Zinke et al. (2019) are ~0.2-0.3 m; however, many uncertainties on vertical offsets measured from OIC along the Kekerengu and Jordan faults are significantly larger (>1 m).

The field measurements in Figure 6c show several *negative* vertical offsets, where the SE side of the Kekerengu Fault was uplifted relative to the NW side. These SE-side up measurements contrast with our offset measurements and those of Zinke et al. (2019); the remote-sensing measurements show consistent uplift of the NW side of the fault except at its NE end. In the region of the fault marked by "CT" in Figure 6c, corrupted data in our pre-earthquake point cloud prevent us from measuring displacements close to the fault. However, a lidar DEM of the area shows a previously-unidentified fault strand SE of the one mapped by Kearse et al. (2018). The two fault strands bound a pressure ridge on the floodplain of the Clarence River. The SE-side up measurements in Figure 6c are on the NW side of this pressure ridge; in the far field (>500 m from the fault), slip on the Kekerengu Fault is clearly NW-side up. Of the other three "negative" vertical offsets measured in the field, two are in a pine plantation ("PP" in Figure 6c) where our method cannot resolve vertical offsets reliably. The third is less than 200 m from another clear NW-side-up offset. The region in which net slip uplifts the SE side of the Kekerengu Fault is thus much smaller than that depicted by Kearse et al. (2018).

We conclude that our offset measurements are generally consistent with field offset measurements and measurements from optical image correlation. Uncertainties on

horizontal offsets can be as low as ~0.2 m where land cover is suitable. Uncertainties on vertical offsets are typically 0.2-0.4 m along the Kekerengu Fault.

5. Surface ruptures in the Seaward Kaikōura Range

We have shown that reliable, high-resolution co-seismic displacements can be extracted from aerial photogrammetry-derived point clouds. To demonstrate the utility of our technique, we now apply it to 2016 surface ruptures in the Seaward Kaikōura Range. High-resolution photogrammetry-derived displacement fields can be used to: (1) map surface ruptures; (2) measure offsets across faults; and (3) constrain fault geometry.

5.1 Mapping surface ruptures

Rupture mapping using high-resolution displacement fields has two main advantages — illustrated in Figure 7 — over the use of post-earthquake lidar and aerial imagery. First, the Snowflake Spur Fault identified by Zinke et al. (2019) is clearly visible in Figure 7b-c, but not in the aerial imagery that Litchfield et al. (2018b) used to map faults in the Seaward Kaikōura Range (neither pre- nor post-earthquake lidar coverage extends to the region of the Snowflake Spur Fault). High-resolution surface displacement fields can therefore be used to map faults that might otherwise be missed using other mapping techniques; the faults mapped by Zinke et al. (2019) and confirmed by this study (blue lines) add ~12 km of fault to maps of the 2016 Kaikōura ruptures. Displacement measurements have the potential to be especially useful when mapping strike-slip offsets with minimal vertical displacements (like the Snowflake Spur Fault), which are hard to identify on lidar hillshades.

Second, many parts of steep, scree-covered mountains are prone to failure during earthquakes; for example, many (>6000) co-seismic landslides occurred in the Seaward Kaikōura Range in 2016 (e.g. Massey et al., 2018). Such (predominantly gravitational) failures can form scarps that are obvious in lidar DEMs and can be interpreted as fault scarps. Using high-resolution displacement fields, it is often possible to distinguish the main fault strand from any subsidiary strands or scarps associated with landslides. For example, many of the white lines in Figure 7c (ruptures mapped from lidar) do not continue further than a few hundred metres along strike. Moreover, some of these mapped

ruptures appear to be mostly gravitational and accommodate minimal strike-slip deformation. The blue lines in Figure 7c — which are mapped from our displacement field — show the locations of major fault strands, including those that accommodate significant strike-slip deformation. Uphill-facing scarps associated with strike-slip and reverse faulting are relatively common in New Zealand and elsewhere (e.g. Eusden et al., 2005; Howard et al., 2005; Stahl et al., 2016); however, it is often difficult to distinguish such scarps from gravitational features like sackungen. Techniques that measure strike-slip offsets — such as point-cloud differencing and optical image correlation — represent an effective way to differentiate between these two sets of commonly-observed features, but only after rupture in an earthquake.

These applications of high-resolution displacement fields are already well documented using differential lidar and OIC (e.g. Avouac et al., 2006; Oskin et al., 2012). Our results show that the resolution of displacements from photogrammetry-derived point clouds can also be sufficient for these applications. Among other applications, constraints on the location of faults from 3D displacement fields could potentially help inform: (1) dynamic models of rupture propagation (e.g. Ando and Kaneko, 2018; Klinger et al., 2018; Ulrich et al., 2019); and (2) models of static stress transfer between faults (e.g. Stein et al., 1997; Mildon et al., 2019). Well-constrained vertical and fault-perpendicular horizontal offsets across faults are especially valuable for these applications, because they can be used to constrain fault dip (Lajoie et al., 2018; Diederichs et al., 2019; Section 5.2).

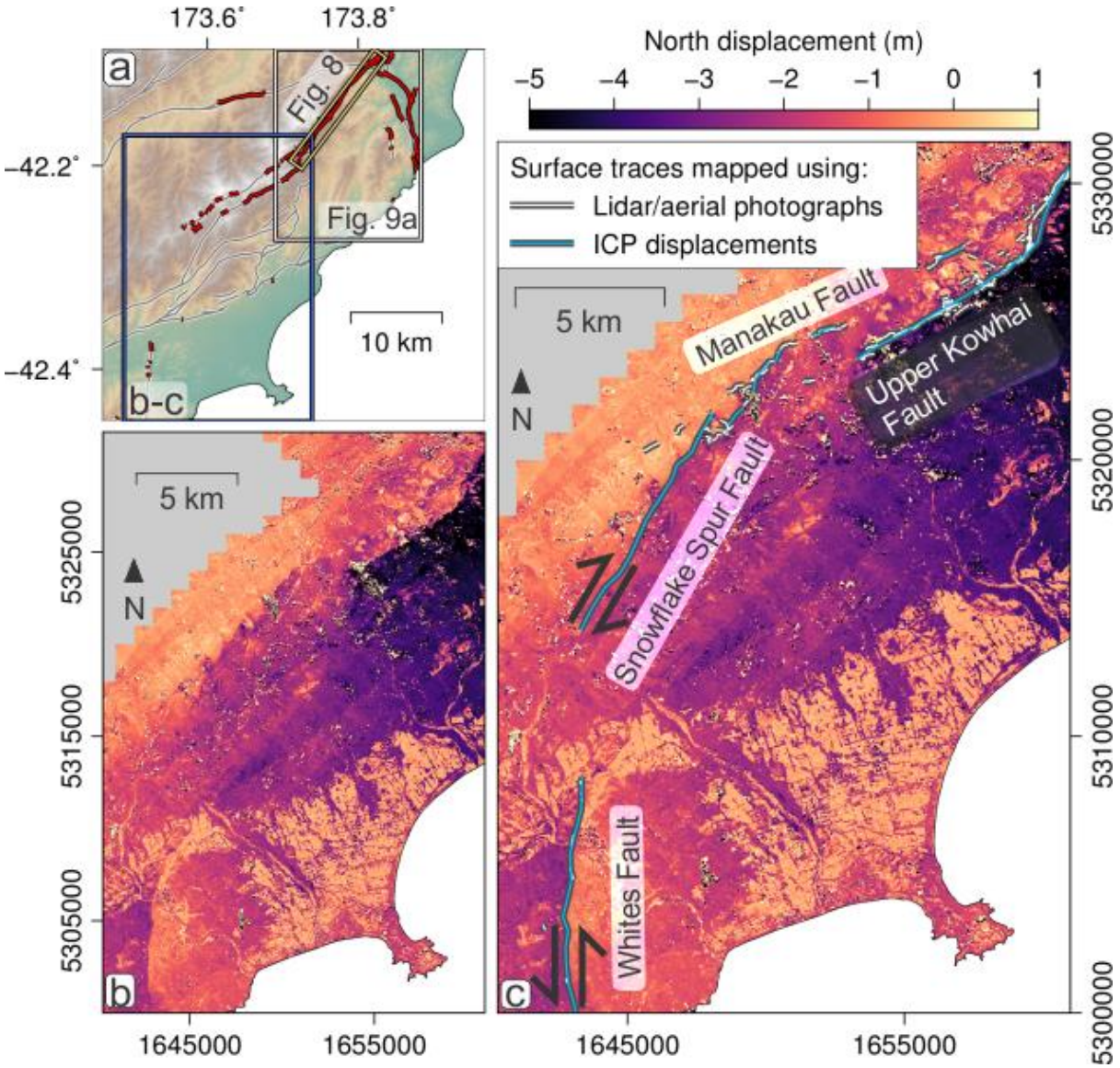

Figure 7. *Utility of our displacement field for rupture mapping.* ***(a)*** *Map showing locations of (b)-(c) and Figure 8.* ***(b)*** *Uninterpreted map of N-S displacements (north positive).* ***(c)*** *Same map as (b) but with surface ruptures mapped from: (1) field observations, a lidar DEM and aerial imagery (white lines; Litchfield et al., 2018b); and (2) our displacement field (blue lines).*

5.2 Slip on the Jordan Fault in 2016

We now discuss the 2016 slip distribution and geometry of two faults in the Seaward Kaikōura Range: the Upper Kowhai Fault and the Jordan Fault (Figure 2a). We focus on the Jordan Fault, investigating apparent differences between 2016 slip on the fault and its long-term behaviour (e.g. Hamling et al., 2017; Litchfield et al., 2018a; Zinke et al., 2019). The Jordan Fault was initially mapped as a NW-dipping reverse fault — the Jordan Thrust — based on Late Holocene offsets (Van Dissen, 1989; Van Dissen and Yeats, 1991). However, in the 2016 earthquake, large normal-sense vertical offsets were observed at the NE end of the fault, near the junction with the Papatea and Kekerengu faults (Hamling et al., 2017). At this NE end, both sides of the fault were uplifted during the Kaikōura earthquake, but the SE side (~6 m) was uplifted much more than the NW side (2-3 m; Hamling et al., 2017; Figure 2). Based on this normal-sense vertical offset, rupture of the Jordan Fault in 2016 has generally been thought to be dextral-normal.

Figure 8b shows offsets in the east, north and vertical directions across the Jordan Fault, measured from swath profiles using the method in Section 3.3. Figure 8c shows horizontal offsets resolved into components parallel to and perpendicular to the local strike of the fault (right-lateral offset and heave). The clear (2-4 m) vertical offsets and heave at the NE end of the Jordan Fault are consistent with dextral-normal slip (Figure 8; Zinke et al., 2019). These large, normal-sense offsets accommodate uplift of the Papatea block along its northern margin. Further SW, vertical and right-lateral offsets across the Jordan Fault are much smaller (typically <1 m and ~4 m respectively); there, the fault heave varies between extensional (normal) and contractional (reverse) offsets (Figure 8c). This spatial alternation between fault-perpendicular horizontal extension and contraction is more consistent with restraining and releasing bends of a predominantly strike-slip fault than a normal-dextral fault.

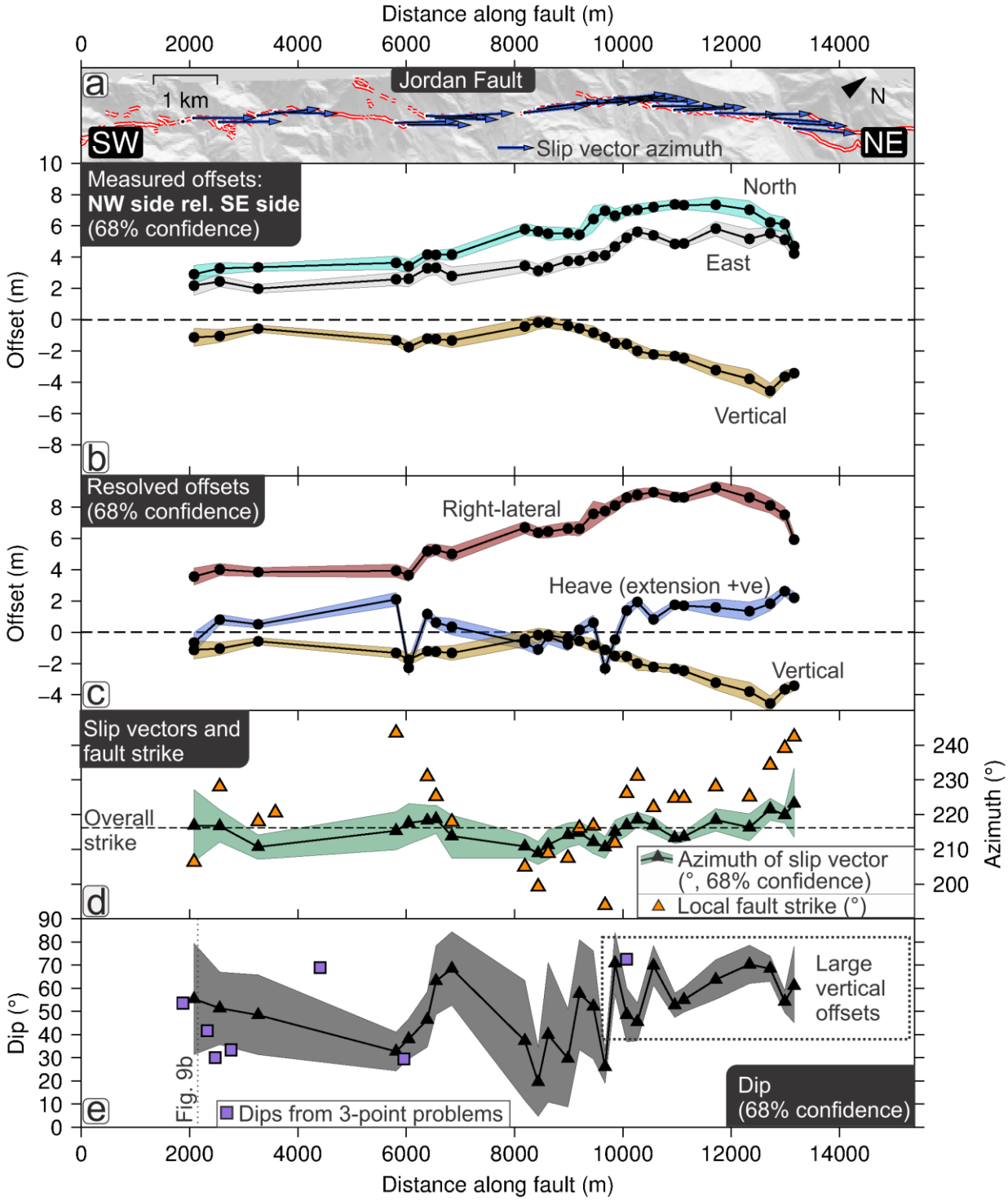

Figure 8. *2016 offsets across the Jordan Fault.* ***(a)*** *Map of surface ruptures (red lines) and measurement site locations along the Jordan Fault. Arrows show horizontal azimuths of slip vectors at each measurement site. Note that arrows show the azimuths of motion of the NW side of the fault relative to the SE side, not the footwall relative to the hanging wall.* ***(b)***

Measured offsets in the E-W, N-S and vertical directions. East, north and up are positive and offsets show the motion of the NW side of the fault (the Seaward Kaikōura Range) relative to the SE side (the Papatea block). ***(c)*** *Horizontal offsets across the fault zone resolved into right-lateral and horizontal fault-perpendicular (heave) components. Fault-perpendicular horizontal extension is positive.* ***(d)*** *Local strike of the fault (orange triangles) and slip-vector azimuths (black triangles) at each measurement site, with 68% confidence envelope for slip-vector azimuths. Note that azimuths have been rotated by 180° relative to (a).* ***(e)*** *Dips calculated from 3D slip vectors and local fault strike at each measurement site (black triangles), with 68% confidence envelope (grey). Purple squares represent the dips of planes calculated from the way mapped surface ruptures cut across topography (lidar DEM), using a three-point-problem approach (Davis et al., 2011).*

Using our 3D offset measurements, we estimate the dip and horizontal slip vector of the Jordan Fault during the 2016 Kaikōura earthquake. Following Lajoie et al. (2019), we estimate dip and slip-vector azimuth at each measurement site separately, using the method described in supplementary text S3. Horizontal azimuths of slip vectors (Figures 8a and 8d) indicate that in 2016, the Jordan Fault accommodated minimal extension or convergence in the horizontal direction perpendicular to its overall strike. Local strikes of surface ruptures (orange triangles in Figure 8d) vary by ~40-50°, but horizontal azimuths of slip vectors are remarkably consistent. The overall strike of the Jordan Fault (dashed line in Figure 8d) passes through the 68%-confidence envelope of almost all of our calculated slip-vector azimuths. The consistency of these slip vectors and the variable occurrence of both fault-perpendicular horizontal contraction and extension (Figure 8c) indicate predominantly strike-slip rupture in 2016. Although the Jordan Fault had previously been thought to have ruptured as a dextral-normal fault in 2016 (e.g. Hamling et al., 2017; Kearse et al., 2018; Litchfield et al., 2018a; Zinke et al., 2019), we conclude that the 2016 earthquake accommodated very little horizontal extension perpendicular to the overall strike of the fault; slip on this fault in 2016 should therefore be treated as a strike-slip rather than a dextral-normal rupture. By contrast, equivalent analysis for the Upper Kowhai Fault (Figure S6) shows consistently-oriented slip vectors that differ in azimuth by

~40° from the overall fault strike. Unlike the Jordan Fault, the Upper Kowhai Fault therefore does appear to have ruptured as a normal-dextral fault in 2016.

At the NE end of the Jordan Fault, there *was* a significant (2-3 m) component of horizontal extension perpendicular to the *local* strike of the fault in 2016, and therefore a normal component of slip. Nevertheless, horizontal azimuths of slip vectors in this region were parallel to the overall strike of the fault. We will discuss the possible significance of this more E-W local strike of the fault in Section 5.3.

For the part of the Jordan Fault where significant vertical offsets were observed (marked by a box in Figure 8e), it is possible to constrain the dip of the fault from offset measurements. Elsewhere, vertical offsets are close to zero and rake must be close to 180°; it is impossible to determine the dip of a plane from a purely fault-parallel slip vector (Lajoie et al., 2019). The well-constrained dip estimates at the NE end of the fault cover a relatively large range but are moderate or steep, between ~50 and 80°. Further SW, vertical offsets and heave were much smaller and estimated dips are consequently less reliable; however, they do generally agree with dips estimated from three-point problems (e.g. Davis et al., 2011) where the fault cuts across topography (purple squares in Figure 8e).

In Section 2, we described a lack of constraints on: (1) the long-term slip behaviour of the Jordan Fault; and (2) the 2016 behaviour of the Papatea block. Our results show that the Jordan Fault ruptured in 2016 as a moderate-to-steeply dipping, predominantly strike-slip fault; our measurements represent a constraint on the 2016 behaviour of the Papatea block, since they indicate minimal convergence or extension on the NW side of the block. These constraints on slip in 2016 may also contribute to an understanding of the long-term behaviour of the Jordan Fault, which we now discuss.

5.3 Reconciling 2016 and longer-term slip on the Jordan Fault

Vertical offsets across the Jordan Fault in 2016 were highly variable (Figures 8b-c); they reached ~3-4 m at the NE end of fault, but were <1 m along most of the fault. Everywhere that significant (>0.5 m) vertical offsets did occur in 2016, the SE side of the Jordan Fault was upthrown relative to its NW side. This SE-side-up behaviour contrasts with the best

evidence — from two different sources — of the sense of long-term vertical offsets across the fault. First, Van Dissen and Yeats (1991) mapped several clear reverse offsets exposed in stream valleys along the SE side of the Seaward Kaikōura Range (Figure 9). These reverse offsets (an example of which is shown in Figure 9b) dip shallowly to the NW and were the main reason why this fault was originally named the Jordan Thrust.

Second, the mountains on the NW side of the Jordan Fault (the Seaward Kaikōura Range, which reaches ~2600 m) are much higher than the ~900-1200 m hills on its SE side (the Papatea Block). It seems very likely that this difference in elevation is maintained through slip on a fault with a reverse component of slip (Van Dissen and Yeats, 1991; Litchfield et al., 2018a; Zinke et al., 2019). Southwest of the Jordan Fault, the western end of the Seaward Kaikōura Range is uplifted in the hanging wall of the Hope Fault (Van Dissen and Yeats, 1991; Barrell, 2015). The highest parts of the Seaward Kaikōura Range are immediately to the NW of the Jordan Fault; the only mapped fault capable of uplifting that part of the range is the Jordan Fault — which must have a long-term reverse offset to do so.

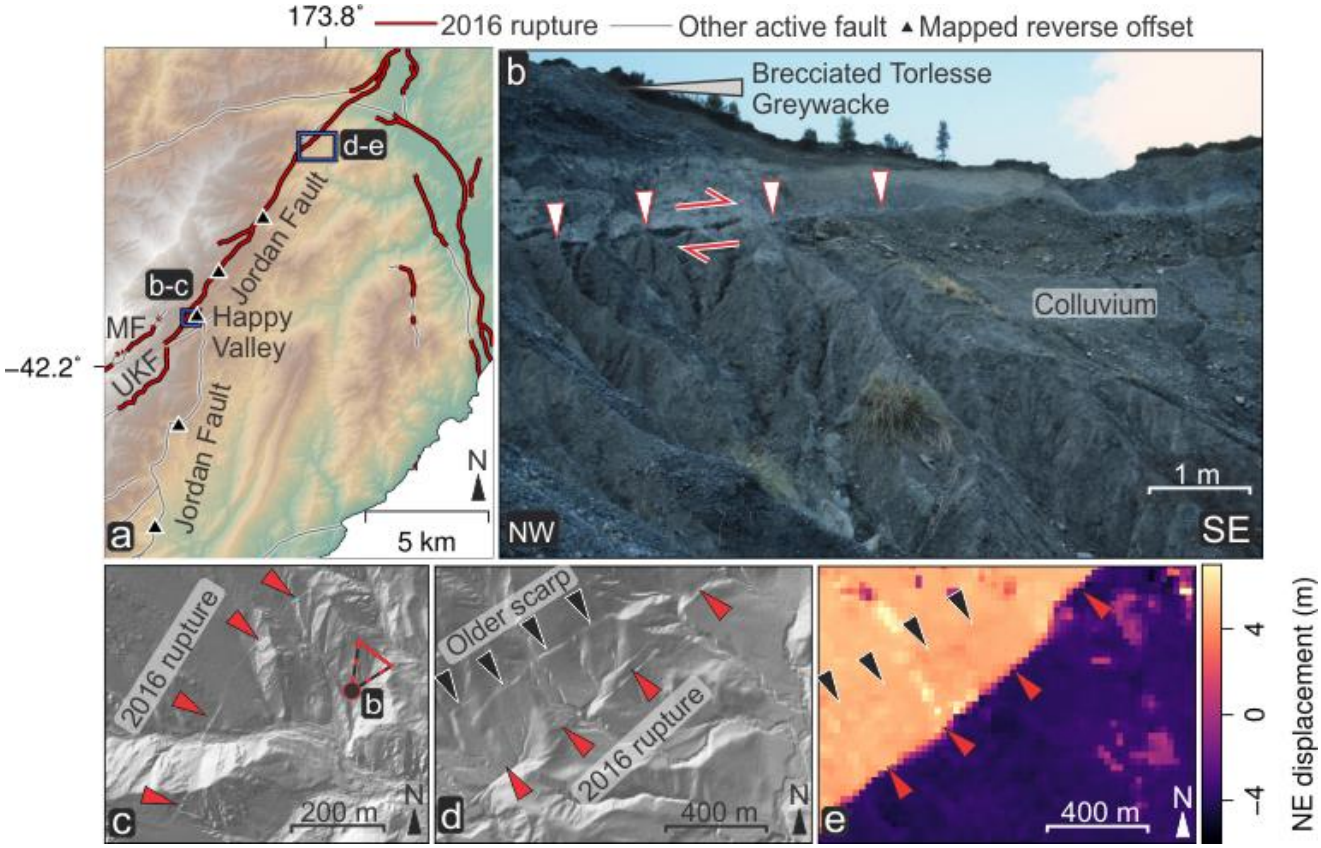

Figure 9. *Strands of the Jordan Fault that did and did not rupture in 2016.* ***(a)*** *2016 ruptures (red, from Litchfield et al., 2018a), other active faults (grey, from Langridge et al., 2016) and reverse offsets in stream banks (black triangles) mapped by Van Dissen and Yeats (1991). Locations of Figures (c), (d) and (e) are marked by blue boxes. MF: Manakau Fault; UK: Upper Kowhai Fault.* ***(b)*** *Side view (looking southeast) of an exposure of the Jordan Fault in Happy Valley (Van Dissen, 1989), showing colluvium overthrust by rocks of the Cretaceous Torlesse Supergroup.* ***(c)*** *Lidar hillshade of Happy Valley, showing the 2016 rupture and the location of (b).* ***(d)*** *Lidar hillshade of the 2016 rupture and a parallel older scarp, which did not rupture in 2016.* ***(e)*** *NE-SW component of displacement (045° direction; NE positive) in the same region as (d), with no significant offset across the older scarp.*

It should be noted that the mapped reverse offsets on the Jordan Fault do not always coincide exactly with the 2016 ruptures; however, the two sets of surface ruptures are close enough to have been formed through slip on the same fault at depth. For example, the surface outcrop of the fault shown in Figure 9b is separated from the 2016 surface rupture by ~220 m. However, the fault plane exposed in Figure 9b appears to dip more shallowly

than the fault plane that ruptured to the surface in 2016: 42° NW for the outcrop in Figure 9a, compared with our steeper estimate of 50-60° NW for the same part of the fault in 2016 (Figure 8e). The two fault planes may therefore join at depth, with different earthquakes rupturing different strands close to the surface. Such partitioning of transpressional deformation into reverse and strike-slip components has been observed for several fault systems in New Zealand and worldwide, at a variety of scales (e.g. Bayasgalan et al., 1999; Eusden et al., 2005; Barth et al., 2012; Lay et al., 2012). The significant distance (~220 m) between the two fault strands highlights the need to consider possible unmapped strands in a fault zone during seismic-hazard assessments. Presently, guidelines from the New Zealand Ministry for the Environment suggest that the region less than 20 m from a mapped fault trace should be classified as a fault avoidance zone (Kerr et al., 2003). Since some faults can rupture different strands in different earthquakes, it may not always be appropriate to rely solely on mapped fault strands to define fault avoidance zones. For example, the Humps Fault (close to the 2016 earthquake epicentre; Figure 1) ruptured an array of mapped, unmapped, and new traces across a ~2.5 km-wide zone in 2016 (Nicol et al., 2018)

Based on the available field and geomorphic evidence, we conclude that long-term slip on the Jordan Fault probably raises the NW side of the fault relative to its SE side. This interpretation of long-term slip requires an explanation for the distribution of vertical offsets observed in 2016, which did not contribute to such a long-term offset. One possible explanation is that the Jordan and Papatea faults do not always rupture together in the same earthquake, as they did in 2016 (Litchfield et al., 2018a; Zinke et al., 2019). In that case, the Jordan Fault could accommodate reverse-dextral motion (and uplift of the Seaward Kaikōura Range) during some (or most) earthquakes, when the Papatea Fault does not rupture. In events where the Papatea and Jordan Faults both rupture — like the 2016 earthquake — the Jordan Fault could behave differently, accommodating both right-lateral motion and uplift of the NW margin of the Papatea block.

The along-strike distribution of vertical offsets across the Jordan fault support this interpretation, in that they are consistent with the accommodation of uplift of the Papatea Block. At its NE end, closest to the Papatea Fault, the SE-side-up vertical offset across the

fault is much larger (~3-4 m) than further SW (~0-1 m); this pattern of vertical offsets fits with the observed decrease in 2016 uplift with distance west of the Papatea Fault (Figure 2; Hamling et al., 2017). Furthermore, the local strike of the Jordan Fault at this NE end is much more E-W (230-240°; Figure 8d) than its overall strike (216°). The combination of this local fault strike and the azimuth of the fault slip vector allows for both: (1) the accommodation of uplift on the SE side of the fault, especially close to the Papatea Fault; and (2) the accommodation of right-lateral motion.

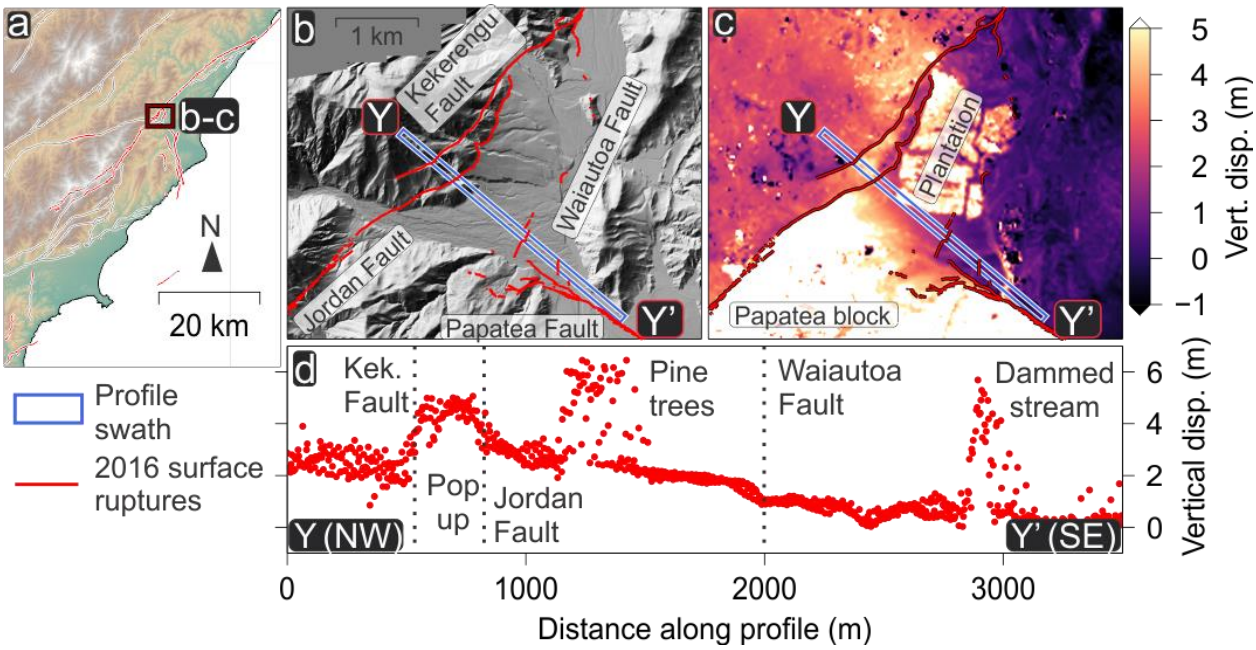

Figure 10. *Vertical displacements at the NE end of the Jordan Fault, near the junction between the Jordan, Kekerengu and Papatea faults.* ***(a)*** *Map showing 2016 ruptures and the location of panels (b) and (c).* ***(b)*** *Lidar hillshade showing the region around the junction of the Jordan, Kekerengu and Papatea faults. Red lines represent mapped 2016 surface ruptures (Langridge et al., 2018) and the blue box shows the outline of swath profile Y-Y'.* ***(c)*** *Vertical displacement field in same region as (b).* ***(d)*** *Profile along the line Y-Y', showing vertical displacements (red circles). Displacements are projected from a 100 m wide swath onto a line along the middle of the profile.*

The north-eastern end of the 2016 rupture of the Jordan Fault continues for ~2 km NE of its junction with the Papatea Fault (Figure 10). That section of the Jordan Fault does not bound the Papatea block; it is also the only place that where the NW side of the fault was upthrown significantly (by ~2 m) in 2016. This NW-side-up behaviour demonstrates that parts of the Jordan Fault can rupture with a reverse of component of slip. However, during the 2016 earthquake, slip on this part of the Jordan Fault does not appear to have contributed significantly to uplift of the Seaward Kaikōura Range. The localised uplift of the NW side of the fault is clearly associated with a 300 m wide pop-up structure between the Kekerengu and Jordan Faults (Figure 10c-d); this 2016 uplift is therefore consistent with the primarily strike-slip behaviour observed along the rest of the Jordan Fault in 2016.

It is unclear what the slip-vector azimuth of any reverse-dextral earthquake on the Jordan Fault would be. However, such an earthquake might *not* involve the southwards motion (by up to ~4 m, relative to stable New Zealand) of the Papatea block and could conceivably accommodate a significant amount of shortening. Immediately SW of the junction between the Jordan and Papatea faults, the weaknesses that ruptured in 2016 strike at ~230-240°; the slip-vector azimuth of any reverse-faulting earthquake would have to differ by at least 25° from the 2016 slip vector to cause shortening across these structures. Alternatively, a reverse-dextral earthquake could rupture weaknesses with a more N-S strike, accommodating NW-SE shortening with a slip vector closer to that of the 2016 event (216°). Such rupture of different fault strands is plausible, especially close to the surface; the reverse offset in Figure 9b-c is ~220 m from the nearest surface rupture. Furthermore, an uphill-facing scarp is present ~200 m north of the 2016 ruptures at the NE end of the fault. Our ICP displacement field shows no (or at least <0.5 m) offset across this ~2 m high scarp (Figure 9e), which almost certainly formed prior to 2016.

This study is not the first to infer significantly different slip behaviour during different earthquakes on the same fault. For example, Cashman and Ellis (1994) observed slickensides with different orientations on the same fault plane. More recently, following the 2013 Balochistan earthquake, Avouac et al. (2014) and Barnhart et al. (2015, 2019) inferred that different earthquakes on the Hoshab Fault in Pakistan accommodated different components of reverse and strike-slip motion. The "bimodal" slip inferred by

these studies appears to be very rare, and in the case of the Hoshab Fault has been questioned (Zhou et al., 2015). Such bimodal slip represents a significant departure from the "characteristic" slip in successive earthquakes inferred for many faults worldwide (e.g. Sieh 1996; Klinger et al., 2011, Zielke et al., 2015); it is therefore important to identify and characterize faults on which bimodal slip is thought to occur, however rare. No paleoearthquake record exists for either the Hoshab or Jordan Fault, so that the slip behaviour of both faults during past earthquakes is not known. However, there is scope to investigate the paleoseismic record of the Jordan Fault.

If — as the best available evidence suggests — the 2016 slip vector on the Jordan Fault differs significantly from that of previous earthquakes on the fault, there are important implications for paleoseismology and seismic hazard (Barnhart et al., 2015). For example, long-term slip rates on faults are often estimated from offsets of geomorphic features like river terraces or fan surfaces (e.g. Fattahi et al., 2006; Langridge et al., 2003; Oskin et al., 2007); the distance that such features are offset represents the cumulative displacement over several earthquakes on the same fault. If the sense of slip on a fault is different in different earthquakes, the cumulative offset of a feature will not reflect the total magnitude of slip on the fault since the feature was formed. Moreover, fault recurrence intervals derived from these long-term slip rates — which are often incorporated into seismic-hazard models and earthquake rupture forecasts (e.g. Stirling et al., 2012, Field et al., 2014) — may be overestimated. Detailed studies of faults that appear to rupture in earthquakes with different characteristics are therefore important and worthwhile. For the case of the Jordan Fault, future paleoseismic studies should help: (1) characterize past earthquakes on the Jordan and Papatea faults; (2) provide constraints on the long-term behaviour of the Jordan fault; and (3) improve understanding of interactions between faults in the Kaikōura region. The remote-sensing measurements described in this and other studies will facilitate comparisons between the 2016 earthquake and previous events.

6. Conclusions

We have demonstrated that high-resolution (0.2-0.3 m) 3D co-seismic displacements can be extracted from point clouds generated from aerial photographs. However, although

differencing of point clouds using the ICP algorithm is an effective way to measure high-resolution co-seismic displacements, it is not the only way. As Figure 6 shows, it is possible to measure horizontal displacements at the same resolution as our ICP results (or better) through optical image correlation. Measurements of vertical displacements from OIC studies are noisier than ICP results but are improving fast (e.g. Kuo et al., 2018; Zinke et al., 2019). Detailed comparisons are required to determine the relative strengths and weaknesses of different techniques, especially with respect to vertical displacements. Without such comparisons, it remains unclear whether ICP point-cloud differencing is the best way to extract 3D displacements from aerial photographs. Nonetheless, we have shown that the technique can be effective; our 3D displacement field is among the best yet created for the area of the 2016 Kaikōura ruptures.

Regardless of the technique used to measure displacements, photogrammetry-derived point clouds represent an exciting opportunity to characterize deformation in future earthquakes. In New Zealand and worldwide, aerial photographic imagery covers a much greater area than lidar. In the absence of pre-earthquake lidar, point clouds derived from aerial and satellite imagery will probably be crucial to studies of future earthquakes.

Based on the available evidence, it appears that co-seismic vertical offsets across the Jordan Fault in 2016 were not consistent with the long-term (Late Quaternary) vertical offset across the fault. The 2016 behaviour of the fault — which did not contribute to relative uplift of the Seaward Kaikōura mountains — may have been unusual, in that the Jordan and Papatea Faults ruptured in the same earthquake. Despite the rugged terrain that the Jordan Fault crosses, it should be possible to obtain a paleoearthquake record for the fault. Such a record would help contribute to understanding of the behaviour of the Jordan Fault and its interactions with neighbouring faults. In the meantime, in paleoseismic studies and seismic-hazard assessments, it is important to consider the possibility that a given fault may rupture differently in different earthquakes.

Acknowledgements

We thank the New Zealand Natural Hazards Research Platform (project 2017-GNS-07) and Land Information New Zealand for funding the capture and processing of the aerial

photographs. Ian Hamling kindly provided us with InSAR-derived 3D displacements to compare with our results. We would like to thank Jarg Pettinga for insightful comments on our displacement fields and Nicola Litchfield for reviewing an earlier version of the manuscript. Alex Morelan and an anonymous reviewer provided helpful reviews, for which we are grateful. Figures were created using the Generic Mapping Tools (Wessel et al., 2013). E.N. was supported by an NSERC Discovery grant and a Canada Research Chair. Measurements of surface offsets across the Kekerengu, Jordan and Upper Kowhai faults are included in Tables S2-S4. Our displacement field is archived on Zenodo (doi: 10.5281/zenodo.3561223), together with ESRI shapefiles and CSV files containing measured fault offsets and uncertainties.

References

Ando, R., & Kaneko, Y. (2018). Dynamic Rupture Simulation Reproduces Spontaneous Multifault Rupture and Arrest During the 2016 M_W 7.9 Kaikoura Earthquake. *Geophysical Research Letters*, *45*(23), 12,875-12,883. https://doi.org/10.1029/2018GL080550

Avouac, J.-P., Ayoub, F., Leprince, S., Konca, O., & Helmberger, D. V. (2006). The 2005, M_W 7.6 Kashmir earthquake: Sub-pixel correlation of ASTER images and seismic waveforms analysis. *Earth and Planetary Science Letters*, *249*(3), 514–528. https://doi.org/10.1016/j.epsl.2006.06.025

Avouac, J.-P., Ayoub, F., Wei, S., Ampuero, J.-P., Meng, L., Leprince, S., et al. (2014). The 2013, M_W 7.7 Balochistan earthquake, energetic strike-slip reactivation of a thrust fault. *Earth and Planetary Science Letters*, *391*, 128–134. https://doi.org/10.1016/j.epsl.2014.01.036

Barnhart, W. D., Briggs, R. W., Reitman, N. G., Gold, R. D., & Hayes, G. P. (2015). Evidence for slip partitioning and bimodal slip behavior on a single fault: Surface slip characteristics of the 2013 M_W7.7 Balochistan, Pakistan earthquake. *Earth and Planetary Science Letters*, *420*, 1–11. https://doi.org/10.1016/j.epsl.2015.03.027

Barnhart, W. D., Gold, R. D., Shea, H. N., Peterson, K. E., Briggs, R. W., & Harbor, D. J. (2019). Vertical Coseismic Offsets Derived From High-Resolution Stereogrammetric DSM Differencing: The 2013 Baluchistan, Pakistan Earthquake. *Journal of Geophysical Research: Solid Earth*, *124*(6), 6039–6055. https://doi.org/10.1029/2018JB017107

Barrell, D. J. A. (2015). *General distribution and characteristics of active faults and folds in the Kaikoura District, North Canterbury* (GNS Science Consultancy Report No. 2014/210).

Barth, N. C., Toy, V. G., Langridge, R. M., & Norris, R. J. (2012). Scale dependence of oblique plate-boundary partitioning: New insights from LiDAR, central Alpine fault, New Zealand. *Lithosphere*, *4*(5), 435–448. https://doi.org/10.1130/L201.1

Bayasgalan, A., Jackson, J., Ritz, J.-F., & Carretier, S. (1999). `Forebergs', flower structures, and the development of large intra-continental strike-slip faults: the Gurvan Bogd fault

system in Mongolia. *Journal of Structural Geology*, *21*(10), 1285–1302. https://doi.org/10.1016/S0191-8141(99)00064-4

Beavan, J., Tregoning, P., Bevis, M., Kato, T., & Meertens, C. (2002). Motion and rigidity of the Pacific Plate and implications for plate boundary deformation. *Journal of Geophysical Research: Solid Earth*, *107*(B10), ETG 19-1-ETG 19-15. https://doi.org/10.1029/2001JB000282

Besl, P. J., & McKay, N. D. (1992). Method for registration of 3-D shapes. In *Sensor Fusion IV: Control Paradigms and Data Structures* (Vol. 1611, pp. 586–606). International Society for Optics and Photonics. https://doi.org/10.1117/12.57955

Bouaziz, S., Tagliasacchi, A., & Pauly, M. (2013). Sparse Iterative Closest Point. In *Proceedings of the Eleventh Eurographics/ACMSIGGRAPH Symposium on Geometry Processing* (pp. 113–123). Aire-la-Ville, Switzerland, Switzerland: Eurographics Association. https://doi.org/10.1111/cgf.12178

Cashman, P. H., & Ellis, M. A. (1994). Fault interaction may generate multiple slip vectors on a single fault surface. *Geology*, *22*(12), 1123–1126. https://doi.org/10.1130/0091-7613(1994)022<1123:FIMGMS>2.3.CO;2

Chen, Y., & Medioni, G. (1992). Object modelling by registration of multiple range images. *Image and Vision Computing*, *10*(3), 145–155. https://doi.org/10.1016/0262-8856(92)90066-C

Clark, K. J., Nissen, E. K., Howarth, J. D., Hamling, I. J., Mountjoy, J. J., Ries, W. F., et al. (2017). Highly variable coastal deformation in the 2016 MW7.8 Kaikōura earthquake reflects rupture complexity along a transpressional plate boundary. *Earth and Planetary Science Letters*, *474*, 334–344. https://doi.org/10.1016/j.epsl.2017.06.048

Davis, G. H., Reynolds, S. J., & Kluth, C. F. (2011). *Structural Geology of Rocks and Regions*. John Wiley & Sons. ISBN: 978-0-471-15231-6.

Diederichs, A., Nissen, E. K., Lajoie, L. J., Langridge, R. M., Malireddi, S. R., Clark, K. J., et al. (2019). Unusual kinematics of the Papatea fault (2016 Kaikōura earthquake) suggest anelastic rupture. *Science Advances*, *5*(10), eaax5703. https://doi.org/10.1126/sciadv.aax5703

Duffy, B., Quigley, M., Barrell, D. J. A., Dissen, R. V., Stahl, T., Leprince, S., et al. (2013). Fault kinematics and surface deformation across a releasing bend during the 2010 MW 7.1 Darfield, New Zealand, earthquake revealed by differential LiDAR and cadastral surveying. *GSA Bulletin*, *125*(3–4), 420–431. https://doi.org/10.1130/B30753.1

Duputel, Z., & Rivera, L. (2017). Long-period analysis of the 2016 Kaikoura earthquake. *Physics of the Earth and Planetary Interiors*, *265*, 62–66. https://doi.org/10.1016/j.pepi.2017.02.004

Ekhtari, N., & Glennie, C. (2018). High-Resolution Mapping of Near-Field Deformation With Airborne Earth Observation Data, a Comparison Study. *IEEE Transactions on Geoscience and Remote Sensing*, *56*(3), 1598–1614. https://doi.org/10.1109/TGRS.2017.2765601

Ekström, G., Nettles, M., & Dziewoński, A. M. (2012). The global CMT project 2004–2010: Centroid-moment tensors for 13,017 earthquakes. *Physics of the Earth and Planetary Interiors*, *200–201*, 1–9. https://doi.org/10.1016/j.pepi.2012.04.002

Elliott, J. R., Nissen, E. K., England, P. C., Jackson, J. A., Lamb, S., Li, Z., et al. (2012). Slip in the 2010–2011 Canterbury earthquakes, New Zealand. *Journal of Geophysical Research: Solid Earth*, *117*(B3). https://doi.org/10.1029/2011JB008868

Elliott, J. R., Walters, R. J., & Wright, T. J. (2016). The role of space-based observation in understanding and responding to active tectonics and earthquakes. *Nature Communications*, *7*, 13844. https://doi.org/10.1038/ncomms13844

Eusden, J. D., Pettinga, J. R., & Campbell, J. K. (2005). Structural collapse of a transpressive hanging-wall fault wedge, Charwell region of the Hope Fault, South Island, New Zealand. *New Zealand Journal of Geology and Geophysics*, *48*(2), 295–309. https://doi.org/10.1080/00288306.2005.9515116

Fattahi, M., Walker, R., Hollingsworth, J., Bahroudi, A., Nazari, H., Talebian, M., et al. (2006). Holocene slip-rate on the Sabzevar thrust fault, NE Iran, determined using optically stimulated luminescence (OSL). *Earth and Planetary Science Letters*, *245*(3), 673–684. https://doi.org/10.1016/j.epsl.2006.03.027

Field, E. H., Arrowsmith, R. J., Biasi, G. P., Bird, P., Dawson, T. E., Felzer, K. R., et al. (2014). Uniform California Earthquake Rupture Forecast, Version 3 (UCERF3)—The Time-Independent Model. *Bulletin of the Seismological Society of America*, *104*(3), 1122–1180. https://doi.org/10.1785/0120130164

Gold, R. D., Clark, D., Barnhart, W. D., King, T., Quigley, M., & Briggs, R. W. (n.d.). Surface Rupture and Distributed Deformation Revealed by Optical Satellite Imagery: The Intraplate 2016 Mw 6.0 Petermann Ranges Earthquake, Australia. *Geophysical Research Letters*, *early view*. https://doi.org/10.1029/2019GL084926

Hamling, I. J., Hreinsdóttir, S., Clark, K., Elliott, J., Liang, C., Fielding, E., et al. (2017). Complex multifault rupture during the 2016 Mw 7.8 Kaikōura earthquake, New Zealand. *Science*, *356*(6334), eaam7194. https://doi.org/10.1126/science.aam7194

Holden, C., Kaneko, Y., D'Anastasio, E., Benites, R., Fry, B., & Hamling, I. J. (2017). The 2016 Kaikōura Earthquake Revealed by Kinematic Source Inversion and Seismic Wavefield Simulations: Slow Rupture Propagation on a Geometrically Complex Crustal Fault Network. *Geophysical Research Letters*, *44*(22), 11,320-11,328. https://doi.org/10.1002/2017GL075301

Hollingsworth, J., Ye, L., & Avouac, J.-P. (2017). Dynamically triggered slip on a splay fault in the Mw 7.8, 2016 Kaikoura (New Zealand) earthquake. *Geophysical Research Letters*, *44*(8), 3517–3525. https://doi.org/10.1002/2016GL072228

Howard, M., Nicol, A., Campbell, J., & Pettinga, J. R. (2005). Holocene paleoearthquakes on the strike-slip Porters Pass Fault, Canterbury, New Zealand. *New Zealand Journal of Geology and Geophysics*, *48*(1), 59–74. https://doi.org/10.1080/00288306.2005.9515098

Jones, E., Oliphant, T., & Peterson, P. (2001). SciPy: Open source scientific tools for Python.

Kaiser, A., Balfour, N., Fry, B., Holden, C., Litchfield, N., Gerstenberger, M., et al. (2017). The 2016 Kaikōura, New Zealand, Earthquake: Preliminary Seismological Report. *Seismological Research Letters*, *88*(3), 727–739. https://doi.org/10.1785/0220170018

Kearse, J., Little, T. A., Dissen, R. J. V., Barnes, P. M., Langridge, R., Mountjoy, J., et al. (2018). Onshore to Offshore Ground-Surface and Seabed Rupture of the Jordan–Kekerengu–Needles Fault Network during the 2016 Mw 7.8 Kaikōura Earthquake, New Zealand. *Bulletin of the Seismological Society of America*, *108*(3B), 1573–1595. https://doi.org/10.1785/0120170304

Kerr, J., Nathan, S., Van Dissen, R., Webb, P., Brunsdon, D., & King, A. (2003). *Planning for development of land on or close to active faults* (New Zealand Ministry for the Environment Report No. 565).

Klinger, Y., Etchebes, M., Tapponnier, P., & Narteau, C. (2011). Characteristic slip for five great earthquakes along the Fuyun fault in China. *Nature Geoscience*, *4*(6), 389–392. https://doi.org/10.1038/ngeo1158

Klinger, Y., Okubo, K., Vallage, A., Champenois, J., Delorme, A., Rougier, E., et al. (2018). Earthquake Damage Patterns Resolve Complex Rupture Processes. *Geophysical Research Letters*, *45*(19), 10,279-10,287. https://doi.org/10.1029/2018GL078842

Lajoie, L. J., Nissen, E., Johnson, K. L., Arrowsmith, J. R., Glennie, C. L., Hinojosa-Corona, A., & Oskin, M. E. (2019). Extent of Low-Angle Normal Slip in the 2010 El Mayor-Cucapah (Mexico) Earthquake From Differential Lidar. *Journal of Geophysical Research: Solid Earth*, *124*(1), 943–956. https://doi.org/10.1029/2018JB016828

Langridge, R. M., Ries, W. F., Litchfield, N. J., Villamor, P., Dissen, R. V., Barrell, D. J. A., et al. (2016). The New Zealand Active Faults Database. *New Zealand Journal of Geology and Geophysics*, *59*(1), 86–96. https://doi.org/10.1080/00288306.2015.1112818

Langridge, Robert M., Rowland, J., Villamor, P., Mountjoy, J., Townsend, D. B., Nissen, E., et al. (2018). Coseismic Rupture and Preliminary Slip Estimates for the Papatea Fault and Its Role in the 2016 Mw 7.8 Kaikōura, New Zealand, Earthquake. *Bulletin of the Seismological Society of America*, *108*(3B), 1596–1622. https://doi.org/10.1785/0120170336

Lay, T., Ye, L., Kanamori, H., Yamazaki, Y., Cheung, K. F., Kwong, K., & Koper, K. D. (2013). The October 28, 2012 Mw 7.8 Haida Gwaii underthrusting earthquake and tsunami: Slip partitioning along the Queen Charlotte Fault transpressional plate boundary. *Earth and Planetary Science Letters*, *375*, 57–70. https://doi.org/10.1016/j.epsl.2013.05.005

Linder, S., Benson, M. L., Myers, B. J., & Raison, R. J. (1987). Canopy dynamics and growth of Pinus radiata.: I. Effects of irrigation and fertilization during a drought. *Canadian Journal of Forest Research*, *17*(10), 1157–1165. https://doi.org/10.1139/x87-179

Litchfield, Nicola J., Villamor, P., Dissen, R. J. V., Nicol, A., Barnes, P. M., Barrell, D. J. A., et al. (2018a). Surface Rupture of Multiple Crustal Faults in the 2016 Mw 7.8 Kaikōura, New Zealand, Earthquake. *Bulletin of the Seismological Society of America*, *108*(3B), 1496–1520. https://doi.org/10.1785/0120170300

Litchfield, N. J., Morgenstern, R., Van Dissen, R. J., Langridge, R. M., Pettinga, J. R., Jack, H., et al. (2018b). *Updated Assessment of Active Faults in the Kaikōura District* (GNS Science Consultancy Report 2018/141).

Little, T. A., Dissen, R. V., Kearse, J., Norton, K., Benson, A., & Wang, N. (2018). Kekerengu Fault, New Zealand: Timing and Size of Late Holocene Surface Ruptures. *Bulletin of the Seismological Society of America*, *108*(3B), 1556–1572. https://doi.org/10.1785/0120170152

MacKenzie, D., Elliott, J., Rhodes, E., Lamb, S., & Parsons, B. (2017). Surface displacements in the 2016 Kaikoura earthquake derived from multi-scale optical data. Presented at the 8th International INQUA Meeting on Paleoseismology, Active Tectonics and Archeoseismology, Blenheim, New Zealand.

Massey, C., Townsend, D., Rathje, E., Allstadt, K. E., Lukovic, B., Kaneko, Y., et al. (2018). Landslides Triggered by the 14 November 2016 Mw 7.8 Kaikōura Earthquake, New Zealand. *Bulletin of the Seismological Society of America*, *108*(3B), 1630–1648. https://doi.org/10.1785/0120170305

Mildon, Z. K., Roberts, G. P., Walker, J. P. F., & Toda, S. (2019). Coulomb pre-stress and fault bends are ignored yet vital factors for earthquake triggering and hazard. *Nature Communications*, *10*(1), 1–9. https://doi.org/10.1038/s41467-019-10520-6

Milliner, C. W. D., Dolan, J. F., Hollingsworth, J., Leprince, S., Ayoub, F., & Sammis, C. G. (2015). Quantifying near-field and off-fault deformation patterns of the 1992 M_W 7.3 Landers earthquake. *Geochemistry, Geophysics, Geosystems*, *16*(5), 1577–1598. https://doi.org/10.1002/2014GC005693

Mitchell, J. S., Mackay, K. A., Neil, H. L., Mackay, E. J., Pallentin, A., & Notman, P. (2012). Undersea New Zealand, 1: 5,000,000. *NIWA Chart, Miscellaneous Series*, *92*.

Moré, J. J. (1978). The Levenberg-Marquardt algorithm: Implementation and theory. In G. A. Watson (Ed.), *Numerical Analysis* (pp. 105–116). Springer Berlin Heidelberg.

Mouslopoulou, V., Saltogianni, V., Nicol, A., Oncken, O., Begg, J., Babeyko, A., et al. (2019). Breaking a subduction-termination from top to bottom: The large 2016 Kaikōura Earthquake, New Zealand. *Earth and Planetary Science Letters*, *506*, 221–230. https://doi.org/10.1016/j.epsl.2018.10.020

Nicol, A., Khajavi, N., Pettinga, J. R., Fenton, C., Stahl, T., Bannister, S., et al. (2018). Preliminary Geometry, Displacement, and Kinematics of Fault Ruptures in the Epicentral Region of the 2016 M_W 7.8 Kaikōura, New Zealand, Earthquake. *Bulletin of the Seismological Society of America*, *108*(3B), 1521–1539. https://doi.org/10.1785/0120170329

Nissen, E., Krishnan, A. K., Arrowsmith, J. R., & Saripalli, S. (2012). Three-dimensional surface displacements and rotations from differencing pre- and post-earthquake LiDAR point clouds. *Geophysical Research Letters*, *39*(16). https://doi.org/10.1029/2012GL052460

Nissen, E., Maruyama, T., Ramon Arrowsmith, J., Elliott, J. R., Krishnan, A. K., Oskin, M. E., & Saripalli, S. (2014). Coseismic fault zone deformation revealed with differential lidar: Examples from Japanese M_W ~7 intraplate earthquakes. *Earth and Planetary Science Letters*, *405*, 244–256. https://doi.org/10.1016/j.epsl.2014.08.031

Oskin, M., Perg, L., Blumentritt, D., Mukhopadhyay, S., & Iriondo, A. (2007). Slip rate of the Calico fault: Implications for geologic versus geodetic rate discrepancy in the Eastern California Shear Zone. *Journal of Geophysical Research: Solid Earth*, *112*(B3). https://doi.org/10.1029/2006JB004451

Oskin, M. E., Arrowsmith, J. R., Corona, A. H., Elliott, A. J., Fletcher, J. M., Fielding, E. J., et al. (2012). Near-Field Deformation from the El Mayor–Cucapah Earthquake Revealed by Differential LIDAR. *Science*, *335*(6069), 702–705. https://doi.org/10.1126/science.1213778

Ragon, T., Sladen, A., & Simons, M. (2018). Accounting for uncertain fault geometry in earthquake source inversions – I: theory and simplified application. *Geophysical Journal International*, *214*(2), 1174–1190. https://doi.org/10.1093/gji/ggy187

Salvatier, J., Wiecki, T. V., & Fonnesbeck, C. (2016). Probabilistic programming in Python using PyMC3. *PeerJ Computer Science*, *2*, e55. https://doi.org/10.7717/peerj-cs.55

Scott, C. P., Arrowsmith, J. R., Nissen, E., Lajoie, L., Maruyama, T., & Chiba, T. (2018). The M7 2016 Kumamoto, Japan, Earthquake: 3-D Deformation Along the Fault and Within the Damage Zone Constrained From Differential Lidar Topography. *Journal of Geophysical Research: Solid Earth*, *123*(7), 6138–6155. https://doi.org/10.1029/2018JB015581

Sieh, K. (1996). The repetition of large-earthquake ruptures. *Proceedings of the National Academy of Sciences*, *93*(9), 3764–3771. https://doi.org/10.1073/pnas.93.9.3764

Socquet, A., Hollingsworth, J., Pathier, E., & Bouchon, M. (2019). Evidence of supershear during the 2018 magnitude 7.5 Palu earthquake from space geodesy. *Nature Geoscience*, *12*(3), 192–199. https://doi.org/10.1038/s41561-018-0296-0

Stahl, T., Quigley, M. C., & Bebbington, M. S. (2016). Tectonic geomorphology of the Fox Peak and Forest Creek Faults, South Canterbury, New Zealand: slip rates, segmentation and earthquake magnitudes. *New Zealand Journal of Geology and Geophysics*, *59*(4), 568–591. https://doi.org/10.1080/00288306.2016.1212908

Stein, R. S., Barka, A. A., & Dieterich, J. H. (1997). Progressive failure on the North Anatolian fault since 1939 by earthquake stress triggering. *Geophysical Journal International*, *128*(3), 594–604. https://doi.org/10.1111/j.1365-246X.1997.tb05321.x

Stirling, M., McVerry, G., Gerstenberger, M., Litchfield, N., Dissen, R. V., Berryman, K., et al. (2012). National Seismic Hazard Model for New Zealand: 2010 Update. *Bulletin of the Seismological Society of America*, *102*(4), 1514–1542. https://doi.org/10.1785/0120110170

Ulrich, T., Gabriel, A.-A., Ampuero, J.-P., & Xu, W. (2019). Dynamic viability of the 2016 Mw 7.8 Kaikōura earthquake cascade on weak crustal faults. *Nature Communications*, *10*(1), 1213. https://doi.org/10.1038/s41467-019-09125-w

Van Dissen, R. J. (1989). *Late Quaternary faulting in the Kaikoura region, southeastern Marlborough, New Zealand* (Masters Thesis). Oregon State University.

Van Dissen, R., Stahl, T., King, A., Pettinga, J., Fenton, C., Little, T. A., et al. (2019). Impacts of surface fault rupture on residential structures during the 2016 Mw 7.8 Kaikōura earthquake, New Zealand. *Bulletin of the New Zealand Society for Earthquake Engineering*, *52*(1), 1–22.

Van Dissen, R. J., & Yeats, R. S. (1991). Hope fault, Jordan thrust, and uplift of the Seaward Kaikoura Range, New Zealand. *Geology*, *19*(4), 393–396. https://doi.org/10.1130/0091-7613(1991)019<0393:HFJTAU>2.3.CO;2

Wallace, L. M., Hreinsdóttir, S., Ellis, S., Hamling, I., D'Anastasio, E., & Denys, P. (2018). Triggered Slow Slip and Afterslip on the Southern Hikurangi Subduction Zone Following the Kaikōura Earthquake. *Geophysical Research Letters*, *45*(10), 4710–4718. https://doi.org/10.1002/2018GL077385

Wang, T., Wei, S., Shi, X., Qiu, Q., Li, L., Peng, D., et al. (2018). The 2016 Kaikōura earthquake: Simultaneous rupture of the subduction interface and overlying faults. *Earth and Planetary Science Letters*, *482*, 44–51. https://doi.org/10.1016/j.epsl.2017.10.056

Wedmore, L. N. J., Gregory, L. C., McCaffrey, K. J. W., Goodall, H., & Walters, R. J. (2019). Partitioned Off-Fault Deformation in the 2016 Norcia Earthquake Captured by Differential Terrestrial Laser Scanning. *Geophysical Research Letters*, *46*(6), 3199–3205. https://doi.org/10.1029/2018GL080858

Wessel, P., Smith, W. H. F., Scharroo, R., Luis, J., & Wobbe, F. (2013). Generic Mapping Tools: Improved Version Released. *Eos, Transactions American Geophysical Union*, *94*(45), 409–410. https://doi.org/10.1002/2013EO450001

Xu, W., Feng, G., Meng, L., Zhang, A., Ampuero, J. P., Bürgmann, R., & Fang, L. (2018). Transpressional Rupture Cascade of the 2016 Mw 7.8 Kaikoura Earthquake, New Zealand. *Journal of Geophysical Research: Solid Earth*, *123*(3), 2396–2409. https://doi.org/10.1002/2017JB015168

Zhou, Y., Elliott, J. R., Parsons, B., & Walker, R. T. (2015). The 2013 Balochistan earthquake: An extraordinary or completely ordinary event? *Geophysical Research Letters*, *42*(15), 6236–6243. https://doi.org/10.1002/2015GL065096

Zhou, Y., Parsons, B. E., & Walker, R. T. (2018). Characterizing Complex Surface Ruptures in the 2013 M_W 7.7 Balochistan Earthquake Using Three-Dimensional Displacements. *Journal of Geophysical Research: Solid Earth*, *123*(11), 10,191-10,211. https://doi.org/10.1029/2018JB016043

Zielke, O., Klinger, Y., & Arrowsmith, J. R. (2015). Fault slip and earthquake recurrence along strike-slip faults — Contributions of high-resolution geomorphic data. *Tectonophysics*, *638*, 43–62. https://doi.org/10.1016/j.tecto.2014.11.004

Zinke, R., Hollingsworth, J., Dolan, J. F., & Van Dissen, R. (2019). Three-Dimensional Surface Deformation in the 2016 M_W 7.8 Kaikōura, New Zealand, Earthquake From Optical Image Correlation: Implications for Strain Localization and Long-Term Evolution of the Pacific-Australian Plate Boundary. *Geochemistry, Geophysics, Geosystems*, *20*(3), 1609–1628. https://doi.org/10.1029/2018GC007951